Granger Causality Inference in EEG Source Connectivity Analysis: A State-Space Approach*

Parinthorn Manomaisaowapak and Anawat Nartkulpat and Jitkomut Songsiri†

Department of Electrical Engineering, Faculty of Engineering

Chulalongkorn University, Bangkok, Thailand 10330

e-mail: parinthorn@gmail.com, anawat.nart0@gmail.com, jitkomut.s@chula.ac.th

October 7, 2020

Abstract

This paper provides a scheme of discovering a brain effective connectivity through EEG signals using a Granger causality (GC) concept characterized on state-space models. We propose a state-space model for explaining coupled dynamics of the source and EEG signals where EEG is a linear combination of sources according to the characteristics of volume conduction. Our formulation has a sparsity prior on the source output matrix that can further classify active and inactive sources. The scheme is comprised of two main steps: model estimation and model inference to estimate brain connectivity. The model estimation consists of performing a subspace identification and the active source selection based on a group-norm regularized least-squares. The model inference relies on the concept of state-space GC that requires solving a discrete-time Riccati equation for the covariance of estimation error. We verify the performance on simulated data sets that represent realistic human brain activities under several conditions including percentages of active sources, a number of EEG electrodes and the location of active sources. The performance of estimating brain networks is compared with a two-stage approach using source reconstruction algorithms and VAR-based Granger analysis. Our method achieved better performances than the two-stage approach under the assumptions that the true source dynamics are sparse and generated from state-space models. The method is applied to a real EEG SSVEP data set and we found that the temporal lobe played a role of a mediator of connections between temporal and occipital areas, which agreed with findings in previous studies.

Keywords: brain connectivity, state-space models, Granger causality, EEG, group sparse structure

*This work has been submitted to the IEEE for possible publication. Copyright may be transferred without notice, after which this version may no longer be accessible.

†Corresponding author

1 Introduction

This paper aims to explore effective connectivity of underlying neural network from EEG signals. It is of great importance in neuroscience to study the direction of network connections among regions of interest (ROI) or neural nodes. Common methods of exploring directional connectivity include dynamic causal modeling (DCM), Granger causality analysis (GC), directed transfer function (DTF), partial directed coherence (PDC) that can be applied to several brain modalities such as EEG, MEG, fMRI; see a recent review in [HAVS+19] and detailed mathematical description of connectivity in [PS16]. In our scope, we limit ourselves to EEG analysis due to the equipment economy compared to other brain acquisitions. If only brain signals on a scalp level are available (that certainly lack of spatial resolution), we explore what more we can improve in effective connectivity analysis. This section describes literature on Granger-based brain connectivity studies examined on EEG signals. It can be categorized into two themes: one that infers brain connectivity of scalp signals and the other that concludes a connectivity in the source space. A conclusion from this survey provides us a guideline to build up our proposed model.

1.1 Connectivity on EEG Signals

This analysis is performed on the scalp EEG signal using a measure of dependence of interest. One typical approach is to fit a VAR model to EEG time series and use a measure such as direct transfer function (DTF) as a dependence measure in [GPO12, §4]. The sensor signals are fitted to a VAR model by least-squares estimation and then Granger causality can be obtained by performing significant tests on VAR coefficients. For example, [ACM+07] learned brain connectivity from VAR coefficients using DTF (directed transfer function), PDC (partial directed coherence) and direct DTF (dDTF) from high-resolution EEG data set. Moreover, a state-space framework can be applied to learn connectivity on sensor space, which is introduced in [STOS17]. The state-space model based on switching vector AR (SVAR) model was introduced for non-stationary time series, a characteristic that has been typical for biological signals. The SVAR model was represented in a state-space representation and the switching parameters were selected by a hidden Markov chain. As a result, the connectivity was learned from PDC that computed from the estimated VAR coefficients. However, it can be shown that this approach could result in *spurious causality* as mentioned in [HNMN13] where no interactions in the source level may lead to substantial interactions in the scalp level.

1.2 Connectivity on reconstructed sources

EEG signals cannot explain the true dynamic of neurons inside the brain because of volume conduction effects. An approach of estimating source time series from EEG signals has been developed and is referred to as *source reconstruction* or *source imaging*. The main idea is to estimate $x(t)$ from the lead-field equation:

$$y(t) = Lx(t) + v(t), \tag{1}$$

where $y(t) \in \mathbf{R}^r$ is the EEG data, $x(t) \in \mathbf{R}^m$ is the source signal, $L \in \mathbf{R}^{r\times m}$ is the *lead field matrix* (given) and $v(t) \in \mathbf{R}^r$ is a measurement noise. The lead-field equation (1) can be used to generate artificial EEG signals when $x(t)$ is simulated (known as *forward problem*). On the other hand, constructing the transmitted signal from the measurements in the above linear equation is often called an *inverse problem*. In order to solve the inverse problem in practice, we note that the lead field matrix varies upon several factors such as locations of EEG sensors, size or geometry of the head, regions of interest (ROIs) and the electrical conductivity of brain tissues, skull, scalp, etc. [SC13]. Examples of existing methods in source reconstruction are Low resolution tomography (LORETA), the weighted minimum-norm estimate (WMN), the minimum-current estimate, linearly constrained minimum-variance (LCMV) beamforming, sparse basis field expansions (S-FLEX) and the focal underdetermined system solution (FOCUSS) [Hau12, §2], [SC13, HNMN13, LWVS15].

In general, the number of EEG channels is lower than the number of sources. Hence, L is generally a fat matrix. As a result, the source imaging problem becomes an underdetermined problem. [MMARPH14] proposed that the source time series matrix is factorized into coding matrix C and a latent source time series $z(t)$, then $x(t) = Cz(t)$ where C is assumed to be sparse. The relationship between sources and sensors is then explained by

$$y(t) = LCz(t) + v(t). \tag{2}$$

The problem of reconstructing x is now to estimate z and C instead. [MMARPH14] applied an $\ell_{2,1}$ regularization method by penalizing the rows of the matrix with the 2-norm to induce a sparsity pattern in source time series. Then the regularized EEG inverse problem with $\ell_{2,1}$-norm penalty term was proposed as

$$\underset{C,Z}{\textbf{minimize}} \quad (1/2)\|LCZ - Y\|_F^2 + \lambda\|C_i^T\|_{2,1} + (1/2)\|Z\|_F^2. \tag{3}$$

The problem is non-convex in C and Z (the matrix of latent time series.) An alternating minimization algorithm can be used for solving a bilinear problem by using initial latents $z(0)$ and approximating rank of C from SVD. Another related approach is [WTO16] that applied sLORETA method to estimate source signals x. PCA was used to reduce dimension of the source signals then the principal source signals $\tilde{x}$ were explained $\tilde{x}(t) = Cz(t)$, resulting in a factor model (2) and the dynamics of $z(t)$ was explained by the VAR model. The dynamics of x can then be explained by the VAR model and VAR coefficients are functions of C.

We note that brain connectivity learned from a source reconstruction approach mainly depends on the performance of the source imaging technique. If the source reconstruction does not perform well, learning brain networks from reconstructed sources could lead to a misinterpretation.

1.3 Connectivity inferred from source and EEG coupled dynamics

This approach considers the dynamics of both source and sensor signals concurrently where the estimation of model parameters can infer brain connectivity directly. The work including [Hau12, HTN$^+$10, GHAEC08, CWM12] considered the same dynamical model that the source signals (x) are explained by a VAR process and EEG signal (y) is a linear combination of the sources as

$$x(t) = \sum_{k=1}^{p} A_k x(t-k) + w(t), \quad y(t) = Lx(t).$$

The technique to estimate unknown sources and lead field matrix (L) from only available mixture EEG data is called *blind source separation*. Independent component analysis (ICA) is one of blind source separation techniques that was used in [Hau12, HTN$^+$10, GHAEC08]. In detail, the ICA technique relies on an assumption that the innovation term of process $w(t)$ must be generalized as a non-Gaussian distribution. [GHAEC08] assumed that the innovation term has both sub and super-Gaussian distribution. Initially, PCA was used to reduce the dimension of EEG data with the assumption that the number of EEG channels was greater than the number of sources. Consequently, the principal EEG signals were fitted to a VAR model directly and ICA was performed on the VAR innovation term for demixing source VAR coefficients. As a result, DTF was computed from the transfer function of the source in the VAR model. However, [GHAEC08] estimated VAR parameters from the sensor signals directly, so the brain connectivity was not sparse due to the volume conduction effect. [Hau12] performed convolutive ICA (CICA) on the innovation term which was assumed to be super-Gaussian hyperbolic secant distributed for ensuring a stable solution. To obtain the sparse source connectivity, model parameters, which are L and A_k's, are estimated using the sum of ℓ_2-regularized maximum-likelihood method. In addition, [Hau12, HTN$^+$10, GHAEC08] assumed that the noise distribution was non-Gaussian, so the decomposition of source signals from ICA had a unique solution. [CWM12] proposed an idea to perform connectivity analysis via state-space models. The state equation was described by *generalized AR model* where the innovation process has a generalized Gaussian distribution. All state-space model parameters were obtained from maximum likelihood estimation. As a result, the relationship between sources was explained by PDC computed from estimated VAR coefficients. [CRTVV10] proposed a state-space framework for finding brain connectivity; however, the sources were assumed to be described by a VAR model. Moreover, [CRTVV10] put some prior information on the lead-field matrix where the cortical regions of interest were known. The dynamical equations are given by

$$x(t) = \sum_{k=1}^{p} A_k x(t-k), \quad y(t) = C\Lambda x(t) + v(t)$$

where C is a known matrix from a prior information on the lead field matrix and Λ is the dipole moment. When formulating the above equation into a state-space form, model parameters including $A_1, \ldots, A_p, \Lambda$ and noise covariance were estimated by expected-maximization (EM) algorithm and then Granger causality can be concluded from the estimated noise covariance. Moreover, a state-space form used in [CRTVV10, CWM12] contains source dynamics described by a VAR model and the observation equation represents a relationship between sources and sensors. The state-space parameters were estimated from maximum likelihood estimation using EM. [YYR16] proposed *a one-step state-space model* estimation framework which aims to find the connectivity in ROI level. The state-space model used in [YYR16] was described by

$$z(t+1) = A(t)z(t) + w(t), \quad x(t) = Pz(t) + \eta(t), \tag{4}$$

$$y(t) = Lx(t) + v(t), \tag{5}$$

where $z(t)$ is a time series for each ROI, $A(t)$ is a VAR coefficient at time t, $x(t)$ is a source time series, P is a binary matrix that determines sources corresponding to its ROIs and $y(t)$ is MEG signal. Hence, the state-space model in [YYR16] is essentially a first-order VAR model. The model parameters and source signals were estimated

using EM algorithm and the ROIs connectivity pattern was explained from the zero pattern in VAR coefficients. [CRTVV10] claimed that the state-space framework was less sensitive to noise than two-stage approaches.

In addition to the above literature, [HBCN$^+$17] did not assume any dynamical models of source and EEG signals but rather estimated the whole source signal directly with a sparse prior on some components of sources. The formulation was a fused lasso with a composite $\ell_{2,1}$ norm regularization and was solved numerically using the ADMM algorithm.

To conclude this section, learning brain connectivity from EEG data can be divided into two main approaches. The first approach explored a causality from EEG data directly (sensor space). However, a connectivity between EEG sensors is not an intrinsic connectivity explaining relationships of neuronal activities in the human brain. The second approach, consisting of *two-stage approach* and *coupled models*, was to learn brain connectivity from source signals (source space). The two-stage approach reconstructed source signals first and often explained source dynamics via VAR models. However, the performance of the two-stage approach highly depended on the performance of source reconstruction. *Coupled models* are then proposed for explaining dynamics of sources and EEG signals concurrently where brain connectivity was discovered from the estimated model parameters. Almost all previous studies assumed that source dynamics are described by a VAR process. As mentioned in [GB19] that neurophysiological data have moving-average components and should be explained by VARMA rather than pure VAR models. This paper presents a generalization of source equation to VARMA and proposes an estimation formulation based on subspace identification with a sparsity prior on the source output matrix. Contributions of this work include the following points.

- Unlike most studies that assumed a VAR process as underlying source dynamics, we consider state-space (or equivalently VARMA process) to explain source equations. Methods of analyzing Granger causality from state-space models are thus needed.
- We adopt the notion of state-space Granger causality from [BS15] and describe theoretical properties that relate to application of views. This includes invariant properties of GC under model coordinate transformation and signal scaling.
- We estimate effective connectivity on a *high-dimensional* source space, as compared to the literature [GHAEC08, GH10, HTN$^+$10, CWM12, HE16a] that only a few of dipoles (≤ 10) were considered.
- The number of sources in the ground-truth system and in the estimated models are often the same in literature. This might not be true in practice. We provide a clear evaluation metric in a fair setting.

2 Background

This section describes state-space equations and the Granger characterization of this model class.

2.1 State-space models

Most literature exploring Granger causality of multivariate time series has relied on the use of VAR models because of its simple causality characterization in model parameters. In this paper, we consider a wider class of linear stochastic processes in the form of state-space models to explain EEG time series dynamics. We assume that source signals ($x \in \mathbf{R}^m$) is an output of state-space model whose state variable is $z \in \mathbf{R}^n$ (or what we call a latent), and the EEG signal ($y \in \mathbf{R}^r$) is a linear combination of the source signals, as described in the following equations.

$$z(t+1) = Az(t) + w(t), \tag{6a}$$
$$x(t) = Cz(t) + \eta(t), \tag{6b}$$
$$y(t) = Lx(t) + v(t). \tag{6c}$$

We call $A \in \mathbf{R}^{n\times n}$ the dynamic matrix, $C \in \mathbf{R}^{m\times n}$ an output matrix mapping the latent to source signal, and $L \in \mathbf{R}^{r\times m}$ is the lead-field matrix determined from a head model. The state noise, w, the output noises η, v are zero-mean and assumed to be mutually uncorrelated.

In EEG applications, the volume conduction explains how the source signal propagates through brain tissues to the EEG signals (here from x to y) and it becomes known that Granger causality learned from y may not be the same pattern as one inferred from x, *i.e.*, spurious effect of Granger causality [dSFK$^+$16]. If model parameters (A, C, L) and noise covariances can be estimated from measurements y then we can consider (6a)-(6b) and conclude a Granger causality in the source signal (x). In what follows, we focus on state equations of the source signal only (6a)-(6b) and discuss how to learn GC of x once all model parameters are estimated.

2.2 Granger causality on state-space models

If one assumes a dynamical equation of a time series as an autoregressive (AR) process, it becomes well-known that Granger causality (GC) is encoded as a common zero pattern of all-lagged AR coefficient matrices. The generalization of this characterization to a state-space equation was provided by [BS15] and is summarized here. As our goal here is to learn a GC of the source time series, only state-space equations (6a)-(6b) are considered. The noise covariance matrices in this system are $W = \mathbf{E}[w(t)w(t)^T]$ (state noise covariance), $N = \mathbf{E}[\eta(t)\eta(t)^T]$ (measurement noise covariance) and $S = \mathbf{E}[w(t)\eta(t)^T]$ (correlation of state and measurement noise).

Granger causality concept is to determine relationships between time series from the covariance of prediction errors. If we denote $\hat{x}(t|t-1)$ the optimal estimator of $x(t)$ in MSE sense, it is a classical result that such optimal predictor of $x(t)$ generated from a state-space model, based on information up to time $t-1$ can be obtained from the Kalman filter. The Kalman filter finds the conditional mean of state variable $z(t)$ based on all available information $\hat{z}(t|t-1) = \mathbf{E}[z(t)|x(t-1),\dots,x(0)]$ and the corresponding covariance of state estimation error is $P(t|t-1) = \mathbf{cov}(z(t) - \hat{z}(t|t-1))$. When the filter is applied in asymptotic sense, P converges to a steady state and satisfies discrete-time algebraic Riccati equation (DARE):

$$P = APA^T - (APC^T + S)(CPC^T + N)^{-1}(CPA^T + S^T) + W. \tag{7}$$

Asymptotically, the covariance of output estimation error is

$$\Sigma = \mathbf{cov}(x(t) - \hat{x}(t|t-1)) = CPC^T + N.$$

We note that if $x \in \mathbf{R}^m$ then $\Sigma \in \mathbf{R}^{m\times m}$ and it is the output estimation error covariance when predicting x using all lagged components in x (full model). To determine an effect of $x_j(t)$ to $x_i(t)$ in Granger sense, we then consider the *reduced model* introduced by eliminating $x_j(t)$ from the full model, and is defined as

$$z(t+1) = Az(t) + w(t), \quad x^R(t) = C^R z(t) + \eta(t),$$

where the superscript R denotes the variable $x(t)$ with j^{th} component eliminated and C^R is obtained by removing the j^{th} row of C. The optimal prediction of $x(t)$ using all information of x except x_j is then also obtained by applying the Kalman filter to the reduced model. We can solve DARE using (A, C^R, W, N^R) and obtain P^R, denoted as the state estimation error covariance and the output estimation error covariance of the reduced model is given by

$$\Sigma^R = C^R P^R (C^R)^T + N^R$$

where N^R is obtained from N by removing the j^{th} row and column of N. We also note that Σ^R has size $(m-1)\times(m-1)$. Doing this way, we can test if x_j is a Granger cause to x_i for all $i \neq j$ by using the Granger measure:

$$F_{ij} \equiv F_{x_j \to x_i | \text{all other } x} = \log\left(\frac{\det \Sigma_{ii}^R}{\det \Sigma_{ii}}\right), \tag{8}$$

where Σ_{ii} and Σ_{ii}^R are the variance of prediction error of $x_i(t)$ obtained from using the full model and the reduced model, respectively. We can repeat the above step for $j = 1, 2, \dots, m$, *i.e.*, learn Granger causality from data by computing F_{ij} for all (i, j) and construct it as a matrix whose diagonals are not in consideration. Subsequently, a significance testing is performed on the off-diagonal entries of this matrix to discard insignificant entries as zeros. We also note that the notation of x_i can be either a single variable or a group of variables and Σ_{ii} has the corresponding dimension of x_i. When x_i is a single variable, then $\det \Sigma_{ii}$ reduces to the diagonal (i, i) entry of Σ. The resulting matrix will be called the Granger causality matrix in this paper.

3 Properties of GC causality

Fundamental properties of GC causality under various transformations are stated in this section. The proofs will be provided in the Appendix B.

Theorem 1. *For VAR process with AR coefficients, $A_1, A_2, \dots, A_p$, we have*

$$F_{ij} = 0 \quad \Leftrightarrow \quad (A_k)_{ij} = 0, \quad k = 1, 2, \dots, p.$$

Proof. An example of proof can be found in [Lüt05]. □

It was shown in [BS15] that a Granger matrix F in (8) can be characterized in the state-space system matrices as well.

$$F_{ij} = 0 \quad \Leftrightarrow \quad C_i^T (A - KC)^k K_j = 0, \tag{9}$$

for $k = 0, 1, \ldots, n$ where C_i^T is the ith row of C, and K_j is the jth column of the Kalman gain given by

$$K = (APC^T + S)(CPC^T + N)^{-1}. \tag{10}$$

We have seen that the Granger causality condition for the VAR model is linear in AR coefficient matrices. Unlike VAR models, GC condition for state-space models is highly nonlinear in system matrices.

Theorem 2. *The following properties of Granger causality hold.*

1. *A GC matrix is invariant under a similarity transform of the system.*
2. *If $C_i^T = 0, S = 0$ and N is diagonal then $F_{ij} = 0$ and $F_{ji} = 0$. As a result, the zeros of F is unchanged when N is changed under a scaling transformation.*
3. *If we permute rows of x to $\tilde{x} = \tilde{C}z + \tilde{\eta}$, then C is row permuted, i.e., $\tilde{C} = \Pi C$ and $\tilde{\eta} = \Pi\eta$. Let $\tilde{\Sigma}$ be the covariance of $\tilde{x}$. We have $\tilde{\Sigma} = \Pi\Sigma\Pi^T$. Moreover, the GC matrix of $\tilde{x}$ under such permutation, is related to F by $\tilde{F} = \Pi F \Pi^T$.*
4. *If $N = 0$ and $S = 0$, then the zero pattern of F is invariant under a scaling transformation of C.*

To interpret the meanings of Theorem 2 we consider the dynamical equations (6a)-(6b) where the aim is to learn GC in variable x. The result in statement 1 is very natural. If one changes a coordinate system of z, this should not affect the causality pattern of x, which is the output of the linear system. For statement 2, if $C_i^T = 0$, it would mean x_i is a pure noise η_i. Then if w and η has no correlation, *i.e.*, $S = 0$, and if η is uncorrelated, *i.e.*, N is diagonal, then the effect of x_i cannot be transmitted to other x_j's by any means. Therefore, no Granger cause from x_i to x_j. Similarly, x_i does not receive any information from other x_j's, so x_i is not Granger caused by x_j. The invariant property of zero pattern in F under a scaling of N has a benefit when one estimates N in the form of $\alpha_n I$ (homogeneous noise) and that is supposed to be a correct structure. Even when an estimated value of α_n can differ from the true value, the estimated zero pattern of F can still be correctly recovered. The statement 3 has an intuitive result. If arranging a list of brain sources in one way corresponds to a certain pattern of Granger causality then shuffling the order of brain sources (*e.g.*, changing the brain coordinate system) leads to permuting the estimated causality pattern. Lastly, statement 4 suggests that an output signal normalization (a typical pre-processing step) can be cast as a scaling transformation of C under noiseless assumption. Such transformation does not change the location of null Granger causality.

4 Proposed method

This section describes the methodology of learning Granger causality patterns from EEG time series data. The method consists of three main processes. From the proposed state-space model in (6), the only available mea-

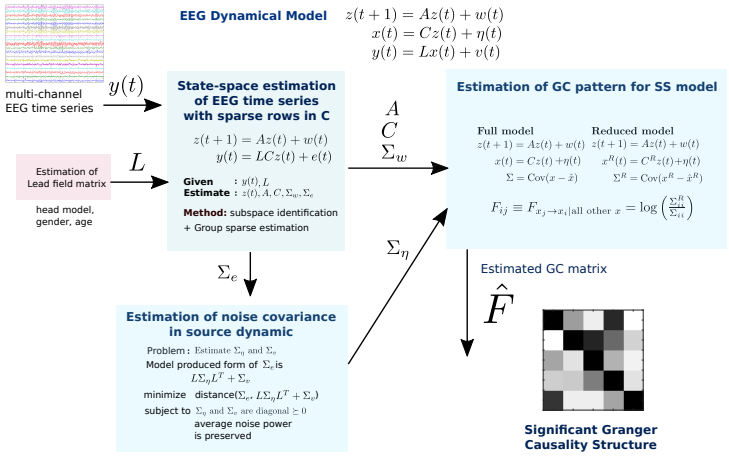

Figure 1: Estimation scheme for learning Granger causality from EEG data based on the proposed model.

surement is EEG signal (y). If we substitute the dynamics of source (x) in the EEG forward equation, we have

$$z(t+1) = Az(t) + w(t), \quad y(t) = LCz(t) + e(t) \tag{11}$$

where $e = L\eta + v$. The matrices Σ_w and Σ_e are noise covariances of w and e, respectively. We can view e as a combination of noises corrupted in the latents and source signals, as perceived at the output equation.

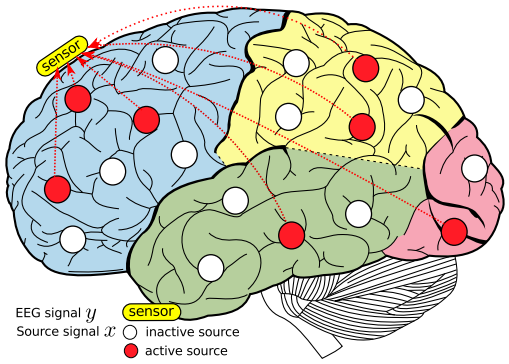

Figure 2: EEG signals are linear combinations of source activities that are assumed to consist of active (red circles) and inactive (white circles) states.

4.1 State-space estimation with sparse rows in output matrix

Given the measurement data of $\{y(t)\}_{t=0}^{N}$, we can estimate state-space parameters A and H in (11) using the *subspace identification method* [OM12] which is available in the system identification toolbox `n4sid` on MATLAB. An estimated state-space model without deterministic input in this toolbox is of the form:

$$z(t+1) = Az(t) + Ke(t), \quad y(t) = Hz(t) + e(t), \tag{12}$$

where K is the Kalman gain matrix and H in (12) takes the form $H = LC$ according to our model (11). This section explains how to estimate A, K, C using a subspace identification technique with a prior structure of C.

Recall from (6b) that the ith source can be interpreted as inactive ($x(t) = 0$) if the ith row of C is entirely zero (in noiseless condition). To incorporate this assumption in the estimation problem, we extend the idea from our prior work [PiS18] based on a regularization technique. We put some prior in C by assuming that *only some sources are active* in a period of time. Consequently, C is *assumed to have some zero rows* corresponding to inactive sources as shown in Figure 2. We therefore propose a subspace identification framework that estimates (A, C) and promotes C to contain some zero rows.

From the subspace (stochastic) identification framework in Theorem 8 of [OM12], the main equation is

$$\begin{bmatrix} \hat{Z}_{i+1} \\ Y_{i|i} \end{bmatrix} = \begin{bmatrix} A \\ H \end{bmatrix} \hat{Z}_i + \begin{bmatrix} \rho_w \\ \rho_e \end{bmatrix} \triangleq \begin{bmatrix} V_1 \\ V_2 \end{bmatrix} = \begin{bmatrix} A \\ LC \end{bmatrix} W + \epsilon, \tag{13}$$

where $\hat{Z}_i$ is the forward Kalman estimate of $\begin{bmatrix} z(i) & z(i+1) & \cdots & z(i+j-1) \end{bmatrix}$, and (ρ_w, ρ_v) are Kalman filter residuals in the innovation form (12). The key success of stochastic subspace identification is to obtain the estimated state sequence directly from the output data via an orthogonal projection. Once $\hat{Z}_i$ and $\hat{Z}_{i+1}$ are computed, we propose to modify the existing algorithm 3 in [OM12] to estimate C in a regularized least-squares sense.

The algorithm of [OM12] involves the extended observability matrix

$$\mathcal{O}_i = \begin{bmatrix} C \\ CA \\ \vdots \\ CA^{i-1} \end{bmatrix} \in \mathbf{R}^{im \times n},$$

and the projection of the row space of Y_f (future output) on the row space of Y_p (past output), denoted by $\xi_i = Y_f / Y_p$; see complete notation details of Y_f, Y_p, Y_f^-, Y_p^+ in the Appendix A. It was proved in Theorem 8 of [OM12] that the Kalman state sequences are related to the projection and the extended observability matrix via

$$\xi_i = \mathcal{O}_i \hat{Z}_i, \quad \xi_{i-1} = Y_f^- / Y_p^+ = \mathcal{O}_{i-1} \hat{Z}_{i+1}.$$

Moreover, by its definition, $\mathcal{O}_{i-1}$ can be obtained by stripping all block rows of $\mathcal{O}_i$ except the last r rows. From this main result, the stochastic algorithm 3 [OM12] is described as follows.

1. Calculate the projections: $\xi_i = Y_f / Y_p$ and $\xi_{i-1} = Y_f^- / Y_p^+$.

2. Calculate the SVD of the weighted projection: $W_1 \xi_i W_2 = U \Sigma V^T \approx U_1 \Sigma_1 V_1^T$ where Σ_1 contains significantly nonzero singular values. The number of nonzero singular values determine the system order.

3. Compute $\mathcal{O}_i = W_1^{-1}U_1\Sigma_1^{1/2}$ and $\mathcal{O}_{i-1}$ is obtained by extracting all rows of $\mathcal{O}_i$ except the last m rows.

4. Determine the estimated state sequences from

$$\hat{Z}_i = \mathcal{O}_i^{\dagger}\xi, \quad \hat{Z}_{i+1} = \mathcal{O}_{i-1}^{\dagger}\xi_{i-1}.$$

Until this step, (A, C) are parameters to be estimated, while other terms in (13) are known, so we propose to estimate A and row-sparse C from the following regularized least-squares problem:

$$\textbf{minimize} \quad \tfrac{1}{2}\|V_1 - AW\|_F^2 + \tfrac{1}{2}\|V_2 - LCW\|_F^2 + \gamma h(C) \tag{14}$$

with variable $A \in \mathbf{R}^{n\times n}$ and $C \in \mathbf{R}^{m\times n}$ whose rows are denoted by C_i^T for $i = 1, 2, \ldots, m$. The problem parameters are V_1, V_2 and $L \in \mathbf{R}^{r\times m}$, the lead-field matrix computed from a head model. The estimation problem (14) is separable in A and C, so A is simply the least-squares solution given by $A = (V_1W^T)(WW^T)^{-1}$.

We propose a group-norm regularization h of the form

$$h(C) = \sum_{i=1}^{m} \|C_i^T\|_2^q, \tag{15}$$

which can be regarded as a composite of ℓ_2 and ℓ_q norms used for promoting *group* sparsity in the row of C. The penalty parameter γ, controls the degree of such sparsity, *i.e.*, when γ is large, C tends to have more sparse rows. Choosing $q = 1$ for h refers to the group lasso problem [HTW15, §3.8]. In this paper, we propose to use $q = 1/2$ which makes h non-convex but this choice has been shown to obtain more desirable properties about the sparsity recovery rate [HLM+17] than using a convex penalty, *e.g.*, when $q = 1$. Solving numerical solutions of the non-convex problem can be challenging. We apply a non-monotone accelerated proximal gradient (nmAPG) method [LL15] and the implementation details are explained in the Appendix C. Choosing a suitable value of γ in an optimal sense is a common issue in any sparse learning approach and we opt to apply model selection criterions such as BIC or AIC [HTF09]. This would require solving (14) with (15) for several values of γ, extracting a sparsity of rows in C for each γ, solving a constrained least-squares subject to such sparsity pattern, and selecting γ that yields the minimum BIC score.

We also consider the well-known ℓ_2-regularization:

$$h(C) = (1/2)\|C\|_F^2 \tag{16}$$

as a baseline method to compare with other estimation approaches. The ℓ_2-regularized least-squares solution of C must satisfy the zero-gradient condition: $L^TLCWW^T + \gamma C = L^TVW^T$. If WW^T is invertible (typically satisfied if we have enough data samples), the optimal condition can be formulated as a Sylvester equation in C:

$$L^TLC + \gamma C(WW^T)^{-1} = L^TVW^T(WW^T)^{-1}, \tag{17}$$

which is linear in C and can be solved by Bartels and Stewart algorithm (implemented in MATLAB and many linear algebra packages). The Sylvester equation has a unique solution if L^TL and $-\gamma(WW^T)^{-1}$ have no common eigenvalues. Such condition holds since L^TL has nonnegative eigenvalues but $-\gamma(WW^T)^{-1}$ always has negative eigenvalues [HJ13, §2]. In conclusion, the ℓ_2 regularized solution of C is unique provided that WW^T is invertible and it can be solved faster than solving (14) with the group-norm regularization. However, it is known that ℓ_2-regularized solutions are not sparse. The solution C tends to zero only when $\gamma \to \infty$; see proof in the Appendix C. The ℓ_2-regularized problem can be a remedy for a constrained least-squares of estimating C with a fixed sparsity pattern in rows of C. It is often that even C is constrained with some zero rows, the remaining nonzero rows still contain too many parameters, resulting in an under-determined system of solving $V_2 = LCW$.

When A and C are estimated, we form the residuals ρ_w, ρ_e in (13) and compute their sample covariances, denoted by Σ_w and Σ_e respectively.

Connection with related work. Our assumption on regarding inactive source from sparse rows in C is in agreement with the use of penalty (15) by [MMARPH14]. However, [MMARPH14] did not model a dynamic of z but rather estimated $z(t)$ as a whole time series segment whereas our subspace approach estimates system parameters but not all related signals directly. The state-space model (4)-(5) by [YYR16] was close to our model (6a)-(6c) but the description of state variable (a time series in ROI level) and the system parameter P (a binary matrix) were different from ours. Moreover, [YYR16] applied EM algorithm in the estimation process due to the presence of latent variables, while we handled this issue by introducing a regularized subspace identification.

4.2 Estimation of noise covariance in the source dynamic

The GC estimation from state-space model parameters explained in Section 2.2 requires information of noise covariances (both state and measurement noises). Consider our methodology in the diagram 1 and the model equations (6a) and (6b). At this step, we have estimated A, Σ_w, C from subspace identification. Then it is left to estimate Σ_η (the measurement noise covariance at the source equation) in order to solve a GC matrix via the Riccati equation.

The measurement noise observed at the output equation (11) has the covariance related to the covariances of η, v by

$$\Sigma_e = L\Sigma_\eta L^T + \Sigma_v. \tag{18}$$

In other words, the RHS of (18) is the model-produced structure form of Σ_e where its value is obtained empirically from the subspace identification described in Section 4.1. The lead field matrix can be obtained from a head model (as part of our assumptions). Therefore, it remains to estimate the unknown Σ_η and Σ_v. Consider the dimensions of all these matrices, where they are symmetric and positive definite, *i.e.*, $\Sigma_e \in \mathbf{S}^r$ and $\Sigma_\eta \in \mathbf{S}^m$ and $\Sigma_v \in \mathbf{S}^r$. Linear equation (18) may have many solutions, so we propose to estimate Σ_η, Σ_v with a certain structure in an optimal sense using the KL divergence distance with a Gaussian assumption.

$$\begin{array}{ll} \textbf{minimize} & (1/2)\,\textbf{tr}(\Sigma_e^{-1}(L\Sigma_\eta L^T + \Sigma_v)) + \log\det(\Sigma_e) - \log\det(L\Sigma_\eta L^T + \Sigma_v) \\ \textbf{subject to} & \Sigma_\eta \succeq 0, \Sigma_v \succeq 0, \\ & \Sigma_\eta = \alpha_\eta I, \quad \Sigma_v = \alpha_v I, \\ & \textbf{tr}(\Sigma_e) = \textbf{tr}(L\Sigma_\eta L^T + \Sigma_v) \end{array} \tag{19}$$

with variables $\Sigma_\eta \in \mathbf{S}^m$ and $\Sigma_v \in \mathbf{S}^r$. We choose to restrict down to a diagonal structure on the variables, corresponding to the assumption that each of the noise vectors η and v is mutually uncorrelated and has a uniform variance (α_η, α_v). In addition, the trace constraint in (19) explains the conservation of the noise average power, *i.e.*, the empirical average power and that of the model-produced form must be equal.

The problem (19) can be further simplified since the variables are merely scalars of α_η and α_v. The trace constraint in (19) gives the linear relation:

$$\alpha_v = -(\textbf{tr}(L^T L)/r)\alpha_\eta + (1/r)\,\textbf{tr}(\Sigma_e) \triangleq -a\alpha_\eta + b, \tag{20}$$

which makes the cost objective in (19) reduced to a function of α_η only. Moreover, the relation between α_η and α_v and the positive constraint on α_v results in the inequality: $0 \le \alpha_\eta \le b/a$. As a result, we can reformulate (19) into a *scalar* optimization problem as

$$\begin{array}{ll} \textbf{minimize} & f(\alpha_\eta) := c\alpha_\eta - \log\det(\alpha_\eta \mathcal{A} + bI) \\ \textbf{subject to} & 0 \le \alpha_\eta \le b/a \end{array} \tag{21}$$

with variable $\alpha_\eta \in \mathbf{R}$ and the problem parameters are $a = \textbf{tr}(L^T L)/r, b = \textbf{tr}(\Sigma_e)/r, c = (1/2)[\textbf{tr}(L^T\Sigma_e^{-1}L) - a\,\textbf{tr}(\Sigma_e^{-1})]$, and $\mathcal{A} = LL^T - aI$. The cost objective of (21) are convex in the variables. In fact, we describe in the Appendix D that solutions of (21) can be obtained almost in a closed-form expression depending on three-case conditions of the problem parameters and the three-case solutions are i) $\Sigma_\eta = 0$, ii) Σ_η has the same average power as Σ_e and iii) the noise power of e is decomposed to Σ_η and Σ_v in an optimal trade-off according to the optimal KL divergence.

If $\Sigma_e \succeq 0$ (degenerated case), then KL divergence is not valid. We estimate Σ_η and Σ_v in a least-squares sense instead. That is, we minimize $\|\Sigma_e - (\alpha_\eta LL^T + \alpha_v I)\|_F^2$ over (α_η, α_v) and the covariance estimates are $\Sigma_\eta = \alpha_\eta I, \Sigma_v = \alpha_v I$.

4.3 Learning significant Granger causality

From the scheme proposed in Figure 1, after we have estimated a Granger causality matrix, $\hat{F}$, one needs to decide which (i, j) entries of F are significantly (or statistically) nonzero. Statistical tests on GC measures characterized from VAR models are available as the log-likelihood ratio test for a nested VAR model or GC inference tests on autocovariance sequence and cross-power spectral density are provided in a MATLAB toolbox by [BS14]. For Granger causality characterized on state-space models, [BS15] concluded that the inference measure in (8) does not have a theoretical asymptotic distribution, while it was observed in their experiments that the test statistics can be well-approximated by a Γ distribution.

As an alternative, a significance testing can be performed using permutation tests or bootstrapping methods. To perform such tests under the null hypothesis that x_j does not Granger cause x_i, it often requires shuffling temporal segments of x_j to examine whether such randomization does not change the effect of x_j to x_i. We note that the permutation is impractical to apply in our context since our proposed scheme does not estimate the

source signal x directly. Alternatively, *Kappa selection* approach [SWF13] is a scheme used in variable selection problem to tune problem parameters (here in our context, a threshold to regard F_{ij} as zero) by a score criterion called *Kappa score*. This method also requires segmenting EEG time series; each of which is used to estimate GC matrix. The work in [PiS19] considered the vectorized version of estimated GC matrices that contain both null and causal entries, and then applied Gaussian mixture models to cluster F_{ij}'s where the group having the least mean was regarded as null GC. The approach in [PiS19] relies on the central limit theorem to conclude that an averaged GC matrix estimated from multi-trial data converges to a Gaussian distribution. A limitation of approaches in this direction is a requirement of repetition of estimation processes on segmented or multi-trial data and hence, a computation power becomes a trade-off.

To the best of our knowledge, a statistical significance test of state-space Granger causality is still an open question where a challenge is on deriving the asymptotic null sampling distribution of the estimator [GB19]. We are aware of the importance of significance testing; however, this paper is not aimed to pursue this topic as it is beyond the paper scope. We will use a heuristic thresholding on discarding small entries of F_{ij}'s. Let $F_{\max}$ and $F_{\min}$ be maximum and nonzero minimum entries of estimated F. A threshold is varied in $(F_{\max} - F_{\min})(0, 1)$ in log scale where the selected threshold is $10^{-6}(F_{\max} - F_{\min})$.

4.4 Generating EEG data

Generating dynamical models is an important step to perform experiments on Granger causality estimation so that we can evaluate the accuracy of estimated GC patterns with ground-truth models. This step is simple in generating VAR processes as a Granger causality is linearly encoded in VAR parameters. In this section, we explain an approach of generating VARMA processes as state-space models where we can control the true GC pattern.

The studies in [BS15, BS11] have shown an important result that GC causality of a filtered VAR process is unchanged if the filter is diagonal, stable and minimum-phase. Let $\tilde{x}(t)$ be a p-lagged VAR process where the z transform relation is given by $\tilde{x} = A(z)^{-1}w$ with VAR polynomial:

$$A(z) = I - (A_1 z^{-1} + A_2 z^{-2} + \cdots + A_p z^{-p}).$$

We consider $G(z)$ an MIMO (multi-input multi-output) transfer function of the form:

$$G(z) = \mathbf{diag}\left(\frac{p_1(z)}{q_1(z)}, \frac{p_2(z)}{q_2(z)}, \ldots, \frac{p_n(z)}{q_n(z)}\right), \tag{22}$$

where each of diagonal entries of G is a rational proper transfer function of a given relative degree. The minimum-phase and stability properties of G suggest that the roots of $p_i(z)$ and $q_i(z)$ must lie inside the unit circle, respectively. As a result, we define $x = G\tilde{x} = G(z)A(z)^{-1}w$ and x is a VARMA process. The result from [BS11] shows that x also has the same GC pattern as $\tilde{x}$, which is easily explained from a zero pattern in VAR coefficients. The system transfer function from w to x can be equivalently represented in a state-space form. Therefore, we proposed a procedure to generate a state-space equation with sparse GC pattern as follows.

1. Generate sparse $A_1, A_2, \ldots, A_p$ matrices randomly with a common zero pattern and the polynomial $A(z)$ must be stable. This is to guarantee that the generated VAR process is stationary. We can do this by randomizing stable roots inside the unit circle and compose the polynomial in the diagonal of $A(z)$. Consequently, off-diagonal entries of A_k's are generated randomly in a common (i, j) location. If the resulting $A(z)$ is not stable, we randomize off-diagonal entries again. In practice, when n is large (in order of several tens or hundred), it is getting more difficult to obtain stable VAR unless the VAR coefficients should be very sparse.

2. Generate a random diagonal transfer function $G(z)$ with required properties. We can generate stable zeros and poles of $G(z)$ when the orders of two polynomials are given.

3. The transfer function from w to x, the desired source signal, is then given by $H(z) = G(z)A(z)^{-1}$. Convert H into a discrete-time state-space form using `tf2ss` command in MATLAB. We obtain (A, B, C, D) of the state-equation: $z(t + 1) = Az(t) + Bw(t), x(t) = Cz(t) + Dw(t)$. Since H is a proper transfer function, we have $D = 0$.

State-space equations and VARMA models can be interchangeably transformed [CGHJ12], so we can refer to the generated model as state-space or VARMA model with sparse GC pattern.

Special case of $G(z)$. As suggested in [BS15] is when $G(z)$ in (22) has the form of a minimum-phase MA polynomial: $G(z) = (1 + cz^{-1})^q I = C(z)I$ with $|c| < 1$, the model reduces to $x = G(z)A(z)^{-1}w = C(z)A(z)^{-1}w = A(z)^{-1}C(z)w$ since $C(z)$ is just a scalar. We can then readily consider x as a VARMA(p, q) process. The AR

and MA coefficients in $A(z)$ and $C(z)$ can be used to convert into a state-space form, for example, the Hamilton form.

As described above, we have generated parameters of ground-truth models of source signals according to (6a) and (6b). It remains to generate a lead field matrix, L, which is computed based on the New York head model described in [HPH16] and select model parameters corresponding to realistic assumptions on EEG signals. We follow implementation details in [HE16a] and add some extensions: i) more number of sources can be considered $m > 2$, ii) source dynamics are VARMA (not VAR) and iii) source time series have an underlying Granger causality, which is generated randomly.

5 Performance evaluation

We aim to evaluate the performance of our method on simulated EEG data sets first. In the data generating process, we can set up model dimensions (n, m, r) and a ground-truth sparsity pattern on the GC matrix associated with such models. In an estimation process, one needs to assume the model dimension; here let $(\tilde{m}, \tilde{n})$ be the number of sources and latents in the estimation which could be larger or smaller than (m, n), while r (the number of EEG channels) is certainly known. Then it leads to a condition in an evaluation procedure since the estimated matrix F of size $\tilde{m} \times \tilde{m}$ could have a different dimension from the ground-truth matrix F. Recall that a ground-truth model used to generate data is explained in (6a)-(6c). We describe how to calculate the classification measures in a fair setting. In this study, we assume that $\tilde{m} > m$ since we can overestimate the number of sources and we expect the source selection procedure to remove inactive sources at the end. By this assumption, $\hat{F} \in \mathbf{R}^{\tilde{m} \times \tilde{m}}$ has a bigger dimension than the true Granger causality matrix $F \in \mathbf{R}^{m \times m}$.

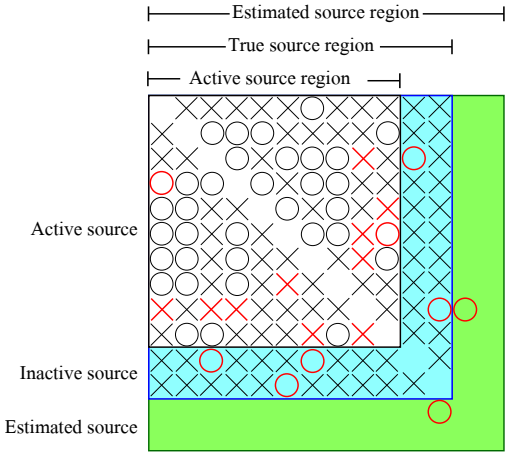

Figure 3: Granger causality evaluation including active source regions, true source region and estimated source region.

Figure 3 shows all three square regions involved in the evaluation process. We start with the **true source region (T)** that contains all the sources in a ground-truth model, and since not all sources are active, a subset called **active source region (A)** consists of all the true active sources where we can reorder the source coordinates so that active sources contain in this region. We define the **estimated source region (E)** as the set of all sources considered in an estimated model. By the assumption that $\tilde{m} > m$, then the true source region must lie inside the estimated source region. By these notations, the set $T - A$ contains all inactive sources in the ground-truth model (highlighted in the blue color), and $E - T$ (green area) represents possible Granger causality that occurred in estimated sources that do not exist in the ground-truth model. The circles $\circ$ denotes the predicted nonzero GC (nonzeros in $\hat{F}$), and the black circles are true positive (TP) and while the red circles are false positive (FP). The cross signs denote the predicted zero GC (zeros in $\hat{F}$), and the red crosses are false negative (FN) while the black crosses are true negative (TN). Hence, when we evaluate an estimated GC matrix $\hat{F} \in \mathbf{R}^{\tilde{m} \times \tilde{m}}$, the following properties hold on the regions shown in Figure 3.

- TP and FN only exist inside the active regions because nonzeros of F in a ground-truth model can only exist in this region.
- True positive rate (TPR) is equal in all regions because the numbers of TP are equal in all regions.
- If all active sources are correctly classified then there is no FP in the true source region and the estimated source region.

- Predicted nonzeros in the green region are regarded as FP since there are no true sources there.
- A fair comparison should be tested on the true source region.
- Accuracy (ACC) and True negative rate (TNR) between regions cannot be compared because the numbers of negatives are different in those regions.
- FP and FN on the estimated source region can only be evaluated when a method is tested on a simulated data sets as the ground-truth models and hence the true source region are known.

From above reasons, the performance on the active true source region reflects how well the method can achieve in TPR. An overall performance of a method can be worse when evaluated on the true source region since if the method predicts any nonzero in the inactive source region, it must be FP. A good method should yield a high TNR on the blue area. Lastly, the performance evaluated on the estimated source region can only drop if the method introduces unnecessary predicted nonzeros in the green area. This arises from two possibilities: error from the source selection algorithm or error from learning significant GC entries.

6 Simulation results

The number of state variables (or latents), sources, and EEG channels in the ground-truth models are denoted by n, m, r, respectively. In the model estimation process, m and n must be set and we use a notation of $(\tilde{n}, \tilde{m})$ (which are not necessarily equal to (n, m). Therefore, $\tilde{L}$ also denotes the lead-field matrix calculated from the parameter $\tilde{m}$. Three main factors to the performance of active source selection and estimating GC causality are as follows.

1. The percentages of active sources in the ground-truth model are set to 20% and 40% with $m = 50$.
2. The number of EEG electrodes varies as $r = 108, 61, 31, 19$.
3. The percentages of deep sources in the ground-truth model varies as $0\%, 50\%, 75\%$.

According to [HE16b], we define eight regions of interest (ROI) that cover left-right, anterior-posterior, and superior-inferior hemispheres, and are labeled as RAI, RAS, RPI, RPS, LAI, LAS, LPI and LPS. Ground-truth models are assumed to contain 8 ROIs and all sources (including both active and inactive) are drawn from 4 ROIs randomly. The first two factors are considered to examine how the performance depends on the sparsity of the ground-truth system and the number of measurements. The third factor is known to affect a performance of localizing active sources. The forth factor, we aim to investigate the robustness of the method when we could wrongly choose the model order in the estimation ($\tilde{m} > m$), which is a common aspect in practice. As we vary the above three factors, we obtain $2 \times 4 \times 3 = 24$ cases to show performances of our source selection and Granger causality learning approach.

For each fixed (n, m, r) and each controlled factor, we randomly generated 100 ground-truth models with different underlying GC causalities and corresponding 100 realizations of EEG time series with SNR of 0.95. All classification performance indices: true positive rate, false positive rate, accuracy, F1 score (TPR, FPR, ACC,F1) are averaged over 100 runs. The ground-truth VARMA models are generated with the sparse VAR part of dimension: $10, 20$, lag of order 2, and the diagonal filter (moving average part) of order 6.

There are many source reconstruction algorithms that can be compared with our source selection scheme (14). Moreover, Granger causality can be estimated from the reconstructed sources from these inverse algorithms using VAR-based approach, as implemented in MVGC toolbox [BS14], and then compared with our estimated state-space Granger causality. For this purpose, we also implemented source reconstruction algorithms including the weighted minimum norm estimator (WMNE), the linear constraint minimum variance beamformer (LCMV), and the standardized low-resolution brain electromagnetic tomography (sLORETA); all implemented in Brainstorm [TBM+11], freely available for online download under the GNU general public license (`http://neuroimage.usc.edu/brainstorm`). In WMNE implementation, the depth weighting is set to 0.5; the regularization parameter of the noise method is set to 0.1 and SNR is fixed as 3. As for LCMV, the noise covariance regularization uses the median value of the eigenvalues. In sLORETA, no depth weighting is applied and SNR is fixed as 3. In the comparative experiments with Brainstorm, we set $(m, r) = (50, 61)$ with 20% active sources and 50% deep sources in ground-truth processes. In our estimation process, we set $\tilde{m} = 100$ and the assumed potential sources are scattered over 8 ROIs of the brain.

All simulation data sets and codes used in this paper are available at `https://github.com/parinthorn/eeg-bc`.

6.1 Selecting active sources

In this experiment we show the performance of classifying active sources. Figure 4 shows a typical example of estimated C when the number of all sources in estimation could be falsely larger than the actual number ($\tilde{m} > m$). The estimated source index i when $i > m$ is regarded as spurious active source if it is incorrectly detected as an active one by inferring from nonzero rows of $\hat{C}$. Our method returned a very small percentage spurious sources in Figure 4 showing a capability of the $\ell_{2,1/2}$ regularized estimation to select sparse rows in C with a good accuracy.

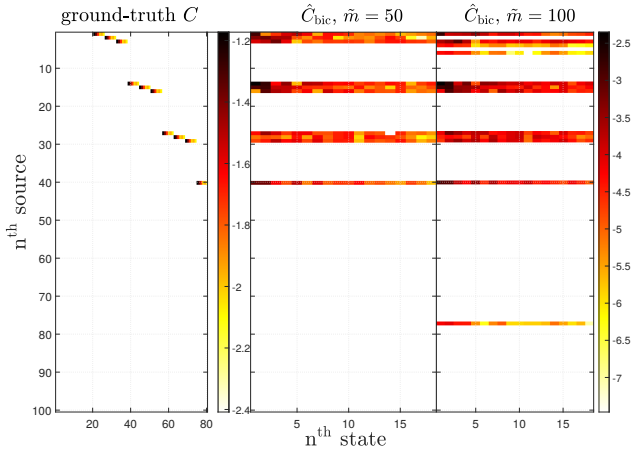

Figure 4: Examples of zero patterns of estimated C as $\tilde{m}$ varies. The color scale is proportional to magnitudes of C_{ij}'s in log scale. The regularized solution of $\hat{C}$ corresponds to the use of λ chosen from BIC. The percentage of deep source is 50% and the number of electrode is 61.

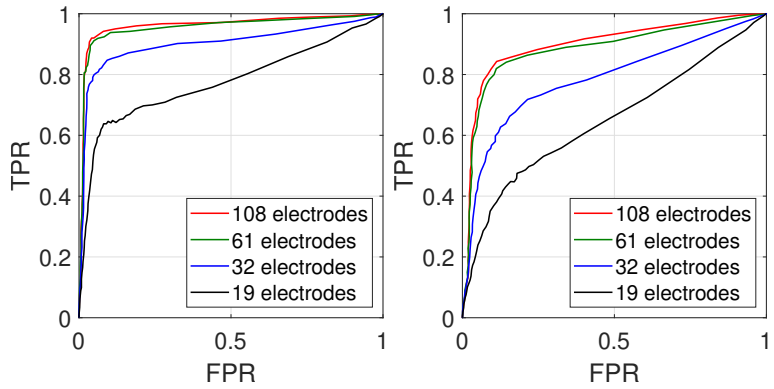

(a) 20% active sources. (b) 40% active sources.

Figure 5: Receiver operation characteristic (ROC) of active and inactive source classification as the number of EEG sensors varies.

Classification performance of the method which depends on λ in the formulation (14) is shown in Figure 5. Each point on ROC curves refers to a classification result from a value of λ, where true positives (negatives) correspond to correctly identified nonzero (zero) rows in $\hat{C}$. The ROC plots show that the performance of classification varies upon the number of EEG channels. As we have more electrode measurements (more data samples), the ROC curve is shifted toward the top left corner (improved accuracy). The results confirm with [SYW+16] that at least more than 64 electrodes are needed for source reconstructions with good quality. Figures 5 (a) show superior performances if the number of active sources is relatively small because a sparsity-inducing formulation (14) generally works well when ground-truth models are sufficiently sparse [HTW15]. Our result in Figure 6 also shows the main factor to source selection performance, which is the location of active sources. As the ratio of deep sources to shallow sources is higher, the smaller area under the ROC curve is obtained.

ROC curves only explain how classification performances vary under the parameter λ. In this experiment, we evaluated the source selection performance when λ was chosen by BIC and displayed it by box plots of TPR, FPR, and ACC in Figure 7 as the distribution of these 100-run metrics may be skewed. TPRs of higher than 80% were mostly obtained when using 61 or 108 electrodes and given that the number of active source is small. Our approach has a great advantage in achieving almost zero FPR when the percentage of active sources is small as seen in Figure 7 (left) that the median of FPR almost goes to zero. When the ground-truth sources are more

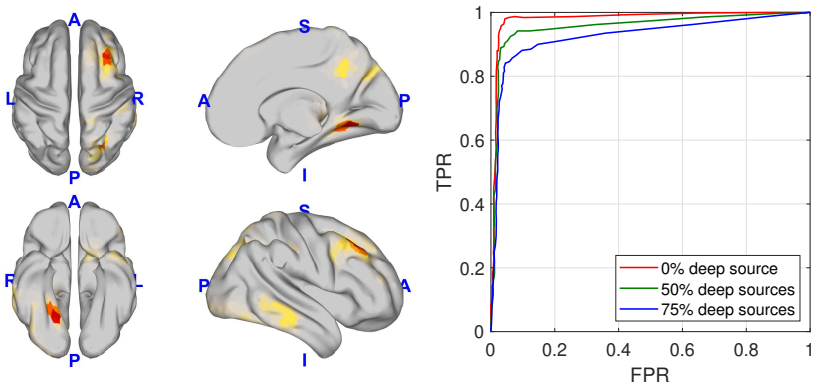

Figure 6: *Left.* An example of ground-truth source locations. *Right.* Receiver operating characteristic (ROC) of active and inactive source classification as varying the percentage of deep sources. The percentage of active sources is 20% and the number of electrodes is 61.

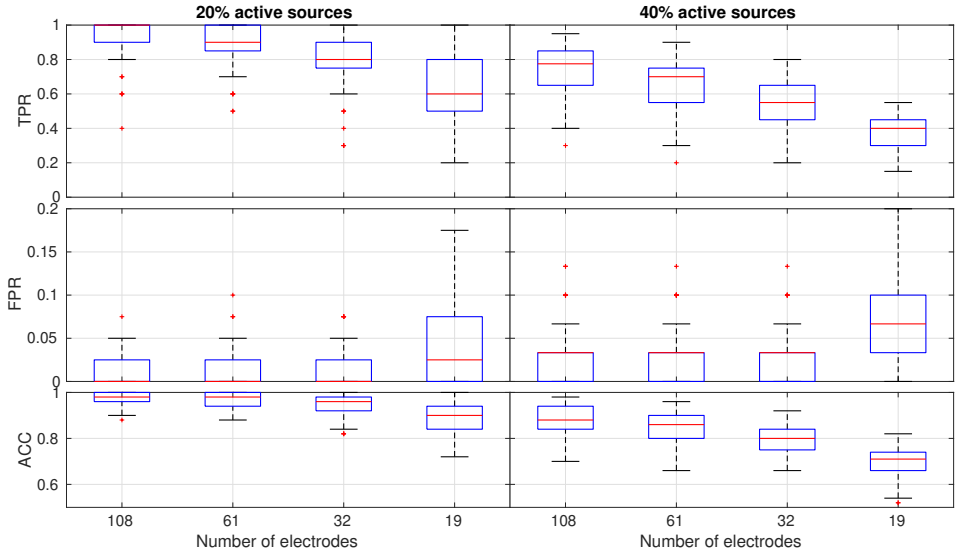

Figure 7: Box plots of source selection performance metrics (TPR, FPR, Accuracy) as the number of electrodes varies and under two conditions of the number of true active sources.

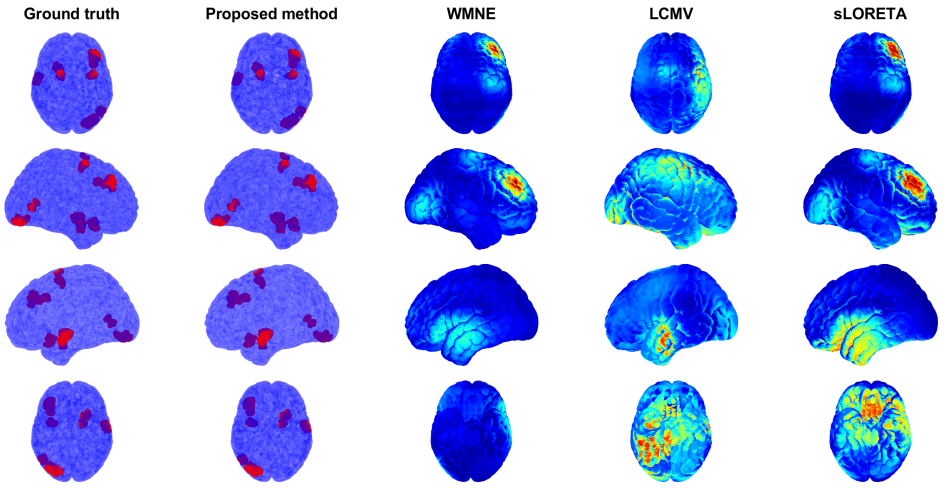

Figure 8: Comparisons with source reconstruction methods: WMNE, LCMV, sLORETA. Our averaged performance indices over 100 runs (of recovering 50 sources) are (TPR,FPR,ACC) $=$ (0.8130, 0.0172, 0.9658).

active, more portions of higher FPRs and TPRs decrease to under 80%. The overall accuracy in the case of 20% active sources is not sensitive much to the number of electrodes, as compared to the case of 40% active sources.

Figure 8 compares source selection results with WMNE, LCMV, and sLORETA. An example from the 25th run out of all 100 samples available in `https://bit.ly/3jAJEeS`, shows that the true active sources can be typically recovered by our method. For source reconstruction algorithms, the ground-truth deep sources in the left hemisphere can be mostly detected by LCMV but not by WMNE and sLORETA. This agrees with a comparison of inverse algorithms given by [APS+19]. It was concluded that when source locations are deep, the overall accuracy of LCMV is higher than eLORETA (which is an improved version of sLORETA) in a high SNR setting (which is the case in this experiment). Results from

6.2 Estimation of Granger causality

The results of discarding inactive sources in section 6.1 showed that if a ground-truth system contains only a few active sources, our method can select the active ones with a good accuracy. In this experiment, we explore Granger causality pattern among the selected active sources. Hence, we show the performance of estimating GC as a binary classification problem (regard F_{ij} as null or causal entry) from simulated EEG signals that were described in section 6. The performance indices, TPR, FPR, ACC and F1 score are reported as three factors (sparsity of ground-truth, percentage of deep sources, and the number of EEG channels) vary.

Our performance of estimating GC was compared to a two-stage approach where a VAR-based GC was learned from reconstructed sources estimated by the inverse algorithms (WMNE, LCMV, sLORETA). We showed this result in a setting that i) the total 50 sources contained 20% active ones, ii) 50% sources were located in deep ROIs and iii) the number of electrodes was 61. In Brainstorm implementation, reconstructed sources in the resolution of 2000K were averaged within each area of 8 ROIs. For GC estimation, the MVGC toolbox [BS14] was implemented using autocovariance method (LWR); VAR lag orders were selected from BIC; significance level of testing VAR-based GC is set to $\alpha = 0.01$. For our method, we set $\tilde{m} = 100$ and sampled these 100 potential sources over 8 ROIs. The method can return an estimated GC matrix in node-based resolution ($\tilde{m} \times \tilde{m}$) or ROI-based resolution (8×8) depending on how we cluster a group of variables (x_i, x_j) in (8).

Figure 9 shows that our method generally performs well when the ground-truth source dynamics contain fewer active sources, according to all metrics. TPR is degraded when the number of electrodes is reduced since we have less data samples. As our formulation and the scheme of selecting the regularization parameter based on BIC favor sparse models, we see that FPR and ACC have small variations as the number of electrodes changes. In overall, the accuracy of sparse ground-truth case is above 95% and not sensitive much to the number of electrodes. In the case of denser ground-truth models (40% active sources), we observed a different trend on FPRs, contrary to the case of 20% active sources. As we use fewer EEG channels, data samples used in estimation were less and BIC tended to select fewer active sources. As stated in (9), the selected zero rows in C always infer zero rows and columns in the GC matrix, *i.e.*, inactive sources have no GC relation with any other sources. This resulted in a trend of decreasing FPRs as the number of electrodes is less. The overall accuracy then had slightly increasing variations in this case. If we focus on the performance of correctly classifying causal entries of a GC matrix, out of all predicted nonzeros, then F1 scores are obtained in the range of $10 - 35\%$, and they are decreasing as the number of electrodes is less. Overall, we obtain accuracy above 90% due to a sparsity-promoted framework in the source selection that allowed us to predict the null entries of GC correctly.

We showed a typical example of estimated GC from the 25th run which is mapped in ROI-based resolution in Figure 10 and the averaged performance over 100 runs in Table 1. The ability to rule out inactive sources in our method helps improve detecting zero entries in the GC matrix. This leads to a significant reduction of false positives as compared to WMNE, LCMV, and sLORETA. Whereas LCMV can relatively recover more deep sources than other inverse algorithms, the inherent moving average dynamics of the ground-truth sources had made it difficult for the VAR-based GC estimation method to accurately recover GC from the reconstructed sources. As we observe from Figure 10, there were biases in strong GC connections inferred from VAR estimates via the two-stage approach. The unexplained moving average dynamic in the residual of estimated source signals can introduce errors in VAR estimates and hence in false GC connections. This is supported by the simulation that while we have set the lag order of the VAR part to 2 in the ground-truth system, the VAR estimation typically picked higher order around 6. In contrast to the two-stage approach, our framework provided a means for estimating VARMA parameters directly in a state-space form. In combination with a prior on sparse rows of C, our method favors sparse GC networks, which further significantly improves overall accuracy, provided that the ground-truth network is also sparse.

Table 1: Averaged performance (and standard deviation) of classifying Granger causality (null versus causal).

Indices	Proposed method	LCMV	WMNE	sLORETA
TPR	0.965 (0.12)	0.885 (0.15)	0.992 (0.05)	0.997 (0.02)
FPR	0.185 (0.14)	0.838 (0.07)	0.979 (0.04)	0.994 (0.01)
ACC	0.829 (0.13)	0.231 (0.07)	0.114 (0.03)	0.101 (0.02)

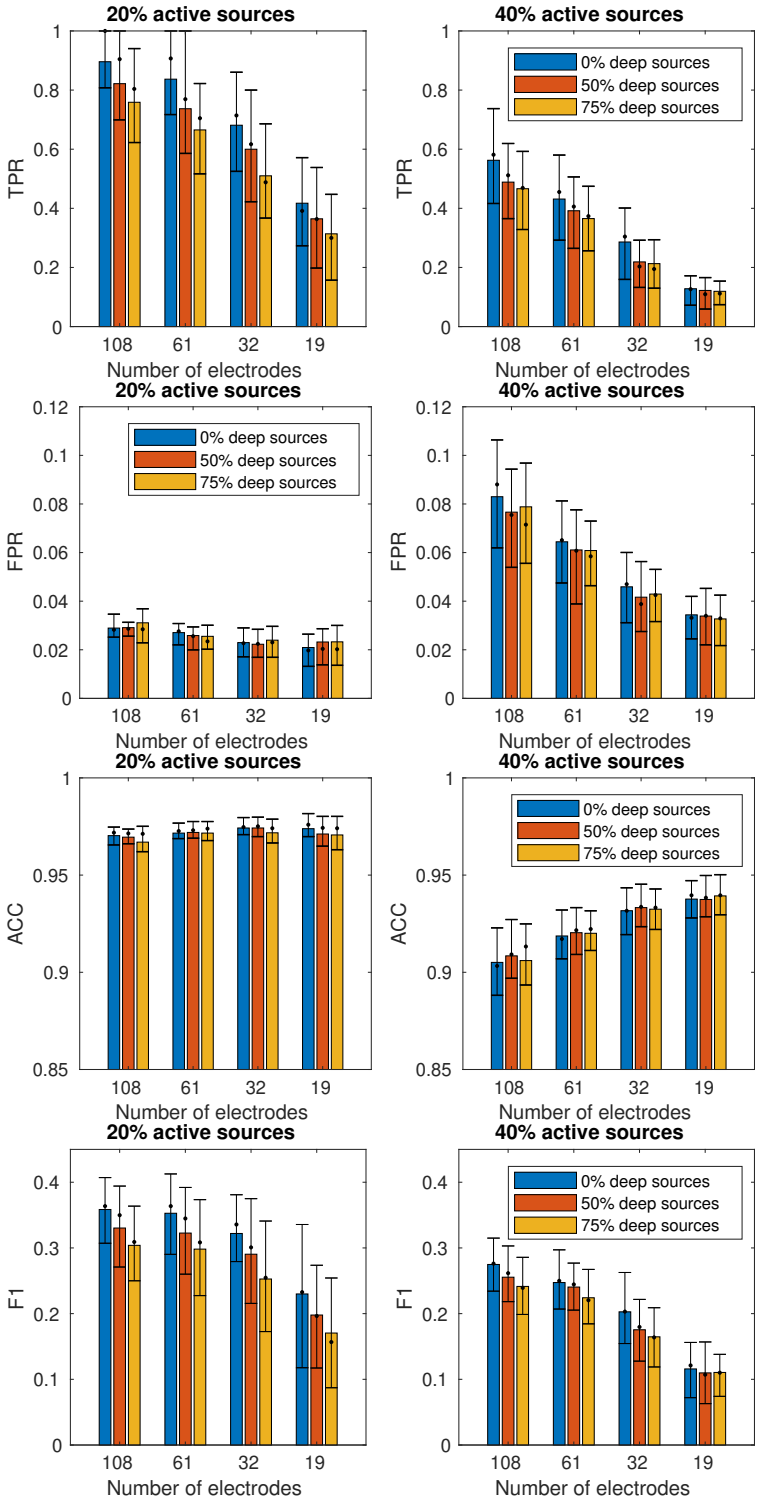

Figure 9: Performance indices of classifying GC causality. The color bar is the averaged performance over 100 runs. The dot is the median and the vertical bar represents the interquartile.

7 Application to real EEG data

In this section, we performed an experiment on real EEG data sets and compare the findings with the previous studies that also explored brain connectivity on this data set with other methods, since the true connectivity is unknown.

Data description. We considered a task-EEG data set containing a steady state visual evoked potential (SSVEP) EEG signals. The data were recorded from a healthy volunteer with flickering visual stimulation at 4 Hz using extended 10-20 system with 30 EEG channels. The data contained three blocks of stimulation and each of the

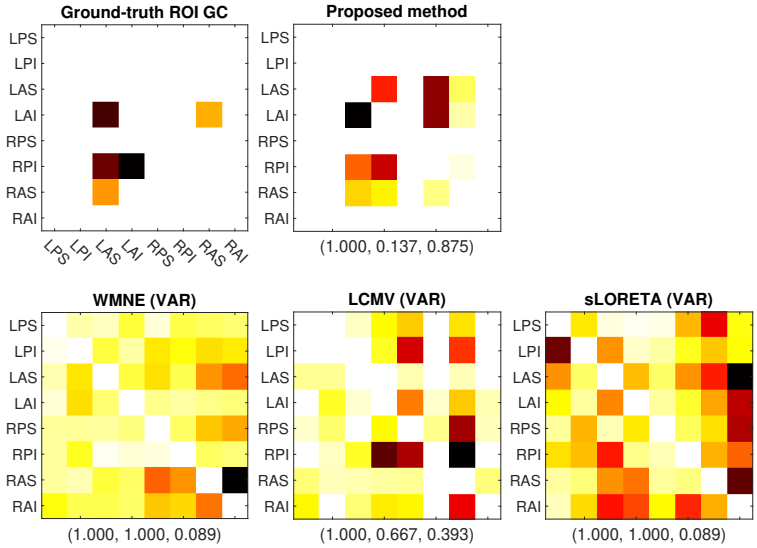

Figure 10: An example of estimated Granger causality. The three numbers in the parenthesis are (TPR,FPR,ACC) of the 25th instance.

stimulation blocks lasted 44.7 seconds. As a result, we obtained 3 trials of task-EEG segments; each of which has $11,126$ time points. The data were collected by Istanbul University, Hulusi Behcet Life Sciences Research Laboratory, Neuroimaging Unit with the approval of the local ethics committee of Istanbul University and the support of the Turkish Scientific and Technological Research Council (TUBITAK) project #108S101.

Experiment setting. The selection of brain sources followed the details in [PLGMBB$^+$18] which included the most actively ranked generators of Occipital lobe, Temporal lobe and Frontal lobe. We sample 18 sources from the six ROIs including

- left Occipital lobe (OL-L), right Occipital lobe (OL-R),
- left Temporal lobe (TL-L), right Temporal lobe (TL-R),
- left Frontal lobe (FL-L), right Frontal lobe (FL-R),

State-space models and source selection process were performed in node-based resolution ($\tilde{m} = 18$). Granger causality was estimated in node-based resolution directly from model parameters. For ROI-based GC, we clustered 18 sources into 3 sources per ROI and redefined x_i in (8) as ROI to compute the estimated GC matrix.

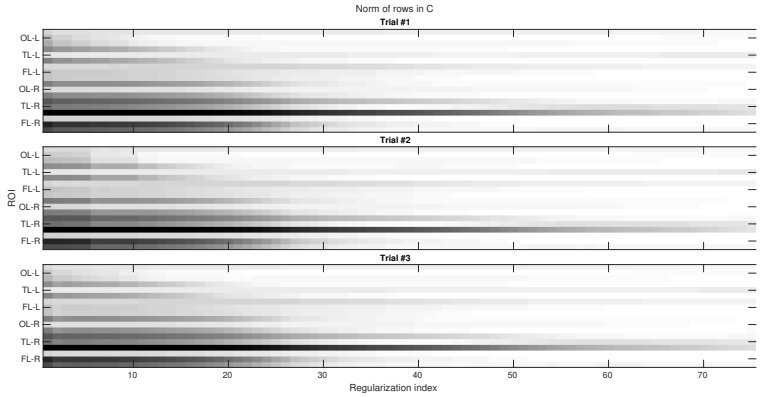

Figure 11: Active source selection results from SSVEP EEG data.

Figure 11 shows active regions as the regularization parameter varies. Strongly active sources appeared in TL-R and FL-R persistently. In Figure 13, we found the second highest connection that flows from FL-L to OL-L and TL-R, and from OL-L to FL-L, OL-R, and TL-R. The linkages of exchanging information from visual cortex in occipital area to frontal lobe is known in SSVEP processing [LTZ$^+$15] where they analyzed the EEG recordings using the proposed double model, compared with the partial directed coherence analysis (PDC), and also concluded this findings with previous studies using fMRI, or MEG. The three-trial estimated GC in Figure 12 shows consistently

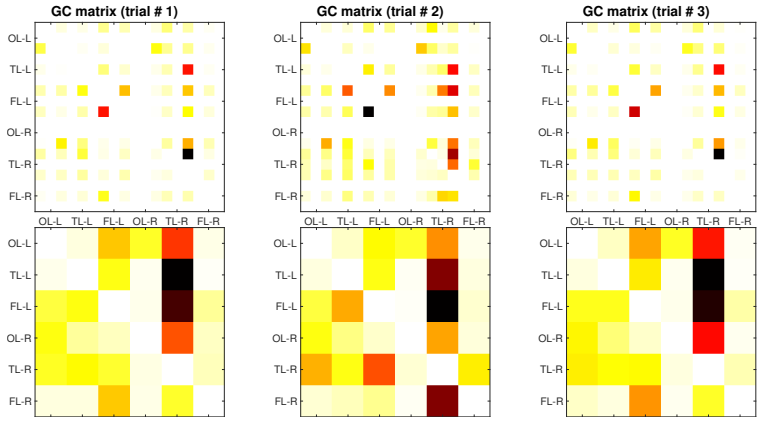

Figure 12: Estimated GC from three trials of SSVEP EEG data. (Top row) Node-based GC. (Bottom row) ROI-based GC.

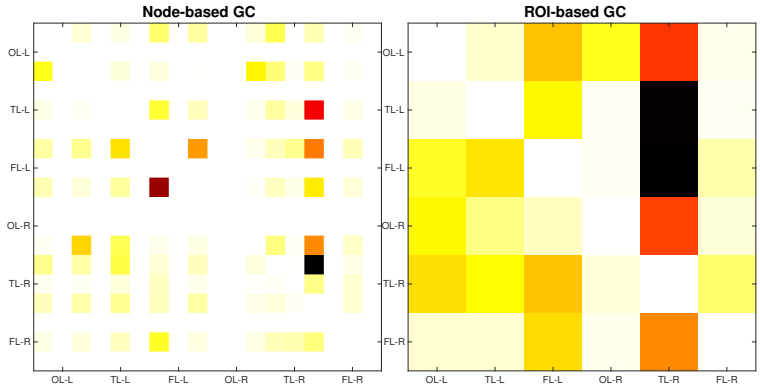

Figure 13: Average of estimated GC over three trials.

that the dominant pathways are from TL-R to regions including OL-L, TL-L, FL-L and OL-R. This is supported by the spatio-temporal analysis in [PLVHRL$^+$17, PLGMBB$^+$18] that the activations in frontal lobe can be preceded by stronger activations in temporal lobe but this was not found in [LTZ$^+$15]. The methods in [PLGMBB$^+$18] was the Hidden Gaussian Graphical State-Model (HIGGS) that relied on a frequency-domain linear state-space model with a sparse connectivity prior. The additional finding that TL played a mediator role in communication between OL and FL, reported in [PLGMBB$^+$18] also agreed with previous studies in the references therein. Our framework can provide a model-based approach to confirm these active regions of exchanging information in visual processing with previous studies.

8 Conclusion

This paper considered an estimation of linear dynamical models for EEG time series and used the model parameters to infer a causality among source signals. The model equations explain coupled dynamics of source signals and scalp EEG signals where only EEG can be measured. The definition of relationships among variables followed the idea of Granger causality (GC) that has been well-established and previously often applied on vector autoregressive (VAR) models. This work extended the VAR models to a more general class, a state-space equation, which led to a highly nonlinear characterization of GC but can be evaluated numerically via solving a discrete Riccati algebraic equation. We have provided analytical results of GC invariant properties under variations system parameters.

In order to estimate such GC matrices, we have proposed a statistical learning scheme consisting of i) subspace identification that promotes a sparse output matrix of source signal, ii) estimation of noise covariances, and iii) the estimation of GC pattern for the obtained state-space model. The subspace identification was extended by using a non-convex regularization to promote sparse rows of C, which can be further used to classify between active and inactive sources. The non-convex penalty was presented as a group norm of ℓ_2 and $\ell_{1/2}$ to obtain a better performance than using a convex penalty in detecting zero rows of C. Given that the models contained equal percentages of deep and shallow sources, the overall best performance was obtained when the ground-truth model had a small portion of active sources. The median of accuracy (based on 100 runs) of classifying active sources ranged in $90-98\%$, which owes to the sparse formulation and the penalty parameter selection using BIC.

When combining all the procedures and evaluating performances of estimating GC, the main factor to overall accuracy is the portion of active sources in the ground-truth models. If the true GC was sparse, the averaged accuracy was around 97% and not sensitive much to the number of electrodes and the location of sources. On the contrary, if the true GC was dense, the overall accuracy slightly degraded to $90 - 94\%$ but had an improving trend when using less electrodes or the ground-truth system contained more deep sources. This contradicts our intuition but can be explained from the characteristic of our sparse learning framework that favors sparse models when the data samples were less available (less electrodes). The resulting sparse C led to sparse GC matrices which helped rule out more FPs, and hence resulted in higher accuracy.

The performance of our method was also evaluated on real SSVEP EEG data whose setting was to stimulate the human brain in the visual cortex area. Results were consistent with previous studies in the sense that a connection is found between occipital and frontal areas which are known to be related to a task of visual processing. Moreover, the temporal lobe was found to be a mediator in the connection between occipital and frontal lobes.

Many practical concerns and limitations of the proposed method can be concluded. Firstly, it requires an approximation of the lead-field matrix (L) which needs information about sensor position, source position, and a head model. In our opinion, the latter appears to be the most uncertain parameter as different subjects would correspond to different head models but this information is unlikely to be exactly known. Secondly, the computational complexity of our method is high in comparison to other non-parametric approaches as the problem (14) is solved with several values of γ before using BIC to select the best model. Lastly, the reported performances were based on thresholding small entries of estimated GC matrices in a heuristic way. We believe that this step can be improved in future work when a statistical test on significant GC is well established, or by considering a framework in machine learning.

Acknowledgment

This research was financially supported by the Research Assistant Scholarship from Graduate School, Chulalongkorn University, and by the Chula Engineering Research grant 2019-2020. Our grateful thanks to Tamer Demiralp, Istanbul University for SSVEP EEG data set, and to Deirel Paz-Linares and Pedro A. Valdés-Sosa for providing supplemental parameters in the SSVEP EEG experiment.

References

[ACM+07] L. Astolfi, F. Cincotti, D. Mattia, M. G. Marciani, L. A Baccala, F. de Vico Fallani, S. Salinari, M. Ursino, M. Zavaglia, L. Ding, et al. Comparison of different cortical connectivity estimators for high-resolution EEG recordings. *Human brain mapping*, 28(2):143–157, 2007.

[APS+19] A. Anzolin, P. Presti, F. Van De Steen, L. Astolfi, S. Haufe, and D. Marinazzo. Quantifying the effect of demixing approaches on directed connectivity estimated between reconstructed EEG sources. *Brain topography*, 32(4):655–674, 2019.

[BS11] L. Barnett and A.K. Seth. Behaviour of Granger causality under filtering: theoretical invariance and practical application. *Journal of neuroscience methods*, 201(2):404–419, 2011.

[BS14] L. Barnett and A. K. Seth. The MVGC multivariate Granger causality toolbox: a new approach to Granger-causal inference. *Journal of neuroscience methods*, 223:50–68, 2014.

[BS15] L. Barnett and A. K. Seth. Granger causality for state-space models. *Physical Review E*, 91(4):1–6, 2015.

[CGHJ12] J. Casals, A. García-Hiernaux, and M. Jerez. From general state-space to VARMAX models. *Mathematics and Computers in Simulation*, 82(5):924–936, 2012.

[CRTVV10] Bing Leung Patrick Cheung, Brady Alexander Riedner, Giulio Tononi, and Barry D Van Veen. Estimation of cortical connectivity from EEG using state-space models. *IEEE Transactions on Biomedical engineering*, 57(9):2122–2134, 2010.

[CWM12] J. Chiang, Z. Jane Wang, and M. J. McKeown. A generalized multivariate autoregressive (GMAR)-based approach for EEG source connectivity analysis. *IEEE Transactions on Signal Processing*, 60(1):453–465, 2012.

[dSFK+16] F. Van de Steen, L. Faes, E. Karahan, J. Songsiri, P.A. Valdes-Sosa, and D. Marinazzo. Critical comments on EEG sensor space dynamical connectivity analysis. *Brain Topography*, pages 1–12, 2016.

[GB19] A.J. Gutknecht and L. Barnett. Sampling distribution for single-regression Granger causality estimators. *arXiv preprint arXiv:1911.09625*, 2019.

[GH10] G. Gómez-Herrero. *Brain connectivity analysis with EEG*. PhD thesis, Tampereen teknillinen yliopisto. Julkaisu-Tampere University of Technology. Publication; 877, 2010.

[GHAEC08] G. Gómez-Herrero, M. Atienza, K. Egiazarian, and J. L. Cantero. Measuring directional coupling between EEG sources. *Neuroimage*, 43(3):497–508, 2008.

[GPO12] R. E. Greenblatt, M. E. Pflieger, and A. E. Ossadtchi. Connectivity measures applied to human brain electrophysiological data. *Journal of Neuroscience Methods*, 207(1):1–16, 2012.

[Hau12] S. Haufe. *Towards EEG Source Connectivity Analysis*. PhD thesis, Technische Universität Berlin, Germany, 2012.

[HAVS+19] B. He, L. Astolfi, P.A. Valdés-Sosa, D. Marinazzo, S.O. Palva, C. Bénar, C.M. Michel, and T. Koenig. Electrophysiological brain connectivity: theory and implementation. *IEEE Transactions on Biomedical Engineering*, 66(7):2115–2137, 2019.

[HBCN+17] L. Albera H. Becker, P. Comon, J.-C. Nunes, R. Gribonval, J. Fleureau, P. Guillotel, and I. Merlet. Sissy: An efficient and automatic algorithm for the analysis of EEG sources based on structured sparsity. *NeuroImage*, 157:157–172, 2017.

[HE16a] S. Haufe and A. Ewald. A simulation framework for benchmarking EEG-based brain connectivity estimation methodologies. *Brain Topography*, pages 1–18, 2016.

[HE16b] S. Haufe and A. Ewald. A simulation framework for benchmarking EEG-based brain connectivity estimation methodologies. *Brain topography*, pages 1–18, 2016.

[HJ13] R. A. Horn and C. R. Johnson. *Matrix Analysis*. Cambridge university press, 2nd edition, 2013.

[HLM+17] Y. Hu, C. Li, K. Meng, J. Qin, and X. Yang. Group sparse optimization via lp,q regularization. *Journal of Machine Learning Research*, 18(30):1–52, 2017.

[HNMN13] S. Haufe, V. V Nikulin, K. Müller, and G. Nolte. A critical assessment of connectivity measures for EEG data: a simulation study. *Neuroimage*, 64:120–133, 2013.

[HPH16] Y. Huang, L.C. Parra, and S. Haufe. The New York Head—A precise standardized volume conductor model for EEG source localization and tES targeting. *NeuroImage*, 140:150–162, 2016.

[HTF09] T. Hastie, R. Tibshirani, and J. Friedman. *The Elements of Statistical Learning: Data Mining, Inference and Prediction*. Springer, 2nd edition, 2009.

[HTN+10] S. Haufe, R. Tomioka, G. Nolte, K. Müller, and M. Kawanabe. Modeling sparse connectivity between underlying brain sources for EEG/MEG. *IEEE Transactions on Biomedical Engineering*, 57(8):1954–1963, 2010.

[HTW15] T. Hastie, R. Tibshirani, and M. Wainwright. *Statistical learning with sparsity: the lasso and generalizations*. Chapman and Hall/CRC, 2015.

[LL15] H. Li and Z. Lin. Accelerated proximal gradient methods for nonconvex programming. In C. Cortes, N. D. Lawrence, D. D. Lee, M. Sugiyama, and R. Garnett, editors, *Advances in Neural Information Processing Systems 28*, pages 379–387. Curran Associates, Inc., 2015.

[LTZ+15] F. Li, Y. Tian, Y. Zhang, K. Qiu, C. Tian, W. Jing, T. Liu, Y. Xia, D. Guo, D. Yao, et al. The enhanced information flow from visual cortex to frontal area facilitates SSVEP response: evidence from model-driven and data-driven causality analysis. *Scientific reports*, 5(1):1–11, 2015.

[Lüt05] H. Lütkepohl. *New Introduction to Multiple Time Series Analysis*. Springer, 2005.

[LWVS15] X. Lei, T. Wu, and P. Valdes-Sosa. Incorporating priors for EEG source imaging and connectivity analysis. *Frontiers in Neuroscience*, 9(284):1–12, 2015.

[MMARPH14] J. Montoya-Martínez, A. Artés-Rodríguez, M. Pontil, and L. K. Hansen. A regularized matrix factorization approach to induce structured sparse-low-rank solutions in the EEG inverse problem. *EURASIP Journal on Advances in Signal Processing*, 19:97, 2014.

[OM12] P. Van Overschee and B. De Moor. *Subspace identification for linear systems: Theory–Implementation–Applications*. Springer Science & Business Media, 2012.

[PiS18] N. Plub-in and J. Songsiri. State-space model estimation of EEG time series for classifying active brain sources. In *2018 11th Biomedical Engineering International Conference (BMEiCON)*, pages 1–5. IEEE, 2018.

[PiS19] N. Plub-in and J. Songsiri. Estimation of Granger causality of state-space models using a clustering with Gaussian mixture model. In *Proceedings of IEEE International Conference on Systems, Man, and Cybernetics (IEEE SMC)*. IEEE, 2019.

[PLGMBB+18] D. Paz-Linares, E. Gonzalez-Moreira, J. Bosch-Bayard, A. Areces-Gonzalez, M.L. Bringas-Vega, and P.A. Valdes-Sosa. Neural connectivity in M/EEG with hidden hermitian Gaussian graphical model. *arXiv:1810.01174 [stat.ME]*, pages 1–34, 2018.

[PLVHRL+17] D. Paz-Linares, M. Vega-Hernandez, P.A. Rojas-Lopez, P.A. Valdes-Hernandez, E. Martínez-Montes, and P.A. Valdes-Sosa. Spatio temporal EEG source imaging with the hierarchical bayesian elastic net and elitist lasso models. *Frontiers in neuroscience*, 11:635, 2017.

[PS16] A. Pruttiakaravanich and J. Songsiri. A Review on Exploring Brain Networks from fMRI Data. *Engineering Journal*, 20(3):1–28, 2016.

[SC13] S. Sanei and J. A. Chambers. *EEG Signal Processing*. John Wiley & Sons, 2013.

[STOS17] S.B. Samdin, C.M. Ting, H. Ombao, and S.H. Salleh. A unified estimation framework for state-related changes in effective brain connectivity. *IEEE Transactions on Biomedical Engineering*, 64(4):844–858, 2017.

[SWF13] W. Sun, J. Wang, and Y. Fang. Consistent selection of tuning parameters via variable selection stability. *The Journal of Machine Learning Research*, 14(1):3419–3440, 2013.

[SYW+16] A. Sohrabpour, S. Ye, G.A. Worrell, W. Zhang, and B. He. Noninvasive electromagnetic source imaging and granger causality analysis: an electrophysiological connectome (econnectome) approach. *IEEE Transactions on Biomedical Engineering*, 63(12):2474–2487, 2016.

[TBM+11] F. Tadel, S. Baillet, J. C. Mosher, D. Pantazis, and R. M Leahy. Brainstorm: a user-friendly application for MEG/EEG analysis. *Computational intelligence and neuroscience*, page 8, 2011.

[WTO16] Y. Wang, C. Ting, and H. Ombao. Modeling effective connectivity in high-dimensional cortical source signals. *IEEE Journal of Selected Topics in Signal Processing*, 10(7):1315, 2016.

[YYR16] M. Tarr Y. Yang, E. Aminoff and K. E Robert. A state-space model of cross-region dynamic connectivity in MEG/EEG. *Advances in Neural Information Processing Systems 29*, pages 1234–1242, 2016.

A Notations in subspace identification

We follow the notations used in [OM12]. First, given output measurements $\{y(t)\}_{t=0}^{N-1}$, we can arrange the sequences in the following matrix.

$$Y_{0|2i-1} = \left[\begin{array}{cccc} y(0) & y(1) & \cdots & y(j-1) \\ y(1) & y(2) & \cdots & y(j) \\ \vdots & \vdots & \vdots & \vdots \\ y(i-1) & y(i) & \cdots & y(i+j+2) \\ \hline y(i) & y(i+1) & \cdots & y(i+j-1) \\ \vdots & \vdots & \vdots & \vdots \\ y(2i-1) & y(2i) & \cdots & y(2i+j-2) \end{array}\right] \triangleq \begin{bmatrix} Y_p \\ Y_f \end{bmatrix}$$

The notation $Y_{0|2i-1}$ represents how we stack output sequences in row and columns so that it can be partitioned at the row i into two blocks of the past (Y_p) and the future (Y_f) output sequences. If $Y_{0|2i-1}$ is row-partitioned

at row $i+1$ then it is denoted by $\begin{bmatrix} Y_p^+ \\ Y_f^- \end{bmatrix}$. From this notation, $Y_{i|i}$ is simply the output sequences starting at time i: $Y_{i|i} = \begin{bmatrix} y(i) & y(i+1) & \cdots & y(i+j-1) \end{bmatrix}$. The index j is typically chosen as $j = N - 2i + 1$ which means that all given data samples are used. In subspace identification, we often encounter the projection of row space of A onto the row space of B, denoted and given by $A/B = AB^T(BB^T)^\dagger B$.

B Proof of GC causality properties

This section provides a proof of Theorem 2.

1. *A Granger causality matrix is invariant under a similarity transform.* **Proof.** A system realization of dynamical equations (6a)-(6b) is parameterized by (A, C) and the noise covariance matrices (W, N). Under a similarity transform to a new coordinate: $\tilde{z} = T^{-1}z$, the dynamic of x is explained by

$$\tilde{z}(t+1) = T^{-1}AT\tilde{z}(t) + T^{-1}w(t),\ x(t) = CT\tilde{z}(t) + \eta(t).$$

Hence, in the new coordinate of state variable, the system has another realization $(\tilde{A}, \tilde{C})$ with a relation $\tilde{A} = T^{-1}AT$ and $\tilde{C} = CT$. Moreover, if we define $\tilde{w} = T^{-1}w$, then noise covariances are

$$\mathbf{cov}\left(\begin{bmatrix} \tilde{w} \\ \eta \end{bmatrix}\right) = \begin{bmatrix} T^{-1}WT^{-T} & T^{-1}S \\ ST^{-T} & N \end{bmatrix}.$$

Let $\tilde{P}$ be the covariance of state estimation error in the new coordinate. It is a straightforward calculation to show that $\tilde{P} = T^{-1}PT^{-T}$ is the solution to DARE (7) and Σ is unchanged under such transformation. Hence, the Granger measure given in (8) is unchanged when it is computed using system matrices corresponding to a new coordinate system.

2. *If $C_i^T = 0, S = 0$ and N is diagonal, then $F_{ij} = 0$ and $F_{ji} = 0$. As a result, the zeros of F is unchanged when N is changed under a scaling transformation.* **Proof.** We will show from the characterization of F_{ij} in (9) where the Kalman gain is given by $K = (APC^T)(CPC^T + N)^{-1}$ when $S = 0$. Let i be the index such that $C_i^T = 0$. It is then obvious that the ith column of APC^T is entirely zero, *e.g.*, $(APC^T)_{si} = 0$ for $s = 1, 2, \ldots, n$. Since N is diagonal, the ith row and the ith column of $CPC^T + N$ is zero, except the (i, i) entry, *e.g.*, $(CPC^T + N)_{ki} = 0$ for $k \neq i$ and $(CPC^T + N)_{ik} = 0$ for $k \neq i$. To see zero pattern of $CPC^T + N$ explicitly, we have

$$CPC^T + N = \begin{bmatrix} & & & 0 & & & \\ & & & \vdots & & & \\ & & & 0 & & & \\ 0 & \cdots & 0 & \times & 0 & \cdots & 0 \\ & & & 0 & & & \\ & & & \vdots & & & \\ & & & 0 & & & \end{bmatrix}. \tag{23}$$

For any invertible X, the (k, i) entry of X^{-1} is related to the M_{ik} (Minor) of X (up to a scaling from $\det X$ and $(-1)^{i+k}$). From the structure given in (23), if we remove either the ith row or the ith column, we see that M_{ij} and M_{ji} of $CPC^T + N$ are all zero. These further imply that $(CPC^T + N)^{-1}_{ki} = 0$ for $k \neq i$ and $(CPC^T + N)^{-1}_{ik} = 0$ for $k \neq i$, *e.g.*, the ith row and the ith column of $(CPC^T + N)^{-1}$ are entirely zero except the (i, i) entry. From the expression of K, we can conclude about its ith column as

$$\begin{aligned} K_{si} &= \sum_{k=1}^{m} (APC^T)_{sk}(CPC^T + N)^{-1}_{ki} \\ &= (APC^T)_{si}(CPC^T + N)^{-1}_{ii} \\ &+ \sum_{k \neq i} (APC^T)_{sk}(CPC^T + N)^{-1}_{ki} \\ &= 0 + 0, \quad s = 1, 2, \ldots, n. \end{aligned}$$

As a result, from an equivalent condition of zero GC in (9), we conclude that $F_{ij} = 0$ since $C_i^T = 0$ and $F_{ji} = 0$ because $K_i = 0$.

3. *If we permute rows of x to $\tilde{x} = \tilde{C}z + \tilde{\eta}$, then C is row permuted, i.e., $\tilde{C} = \Pi C$ and $\tilde{\eta} = \Pi\eta$. Let $\tilde{\Sigma}$ be the covariance of $\tilde{x}$. We have $\tilde{\Sigma} = \Pi\Sigma\Pi^T$. Moreover, the GC matrix of $\tilde{x}$ under such permutation, is related to F by $\tilde{F} = \Pi F\Pi^T$.* **Proof.** If we permute x then the noise covariances become

$$\mathbf{cov}\left(\begin{bmatrix} w \\ \tilde{\eta} \end{bmatrix}\right) = \begin{bmatrix} W & S\Pi^T \\ \Pi S & \Pi N\Pi^T \end{bmatrix}.$$

When solving DARE (7) with $\tilde{C}$ and the new covariances: $S\Pi^T$ and $\Pi N\Pi^T$, we can see that the solution P to DARE is unchanged. As a result, $\tilde{\Sigma} = \tilde{C}P\tilde{C}^T + \tilde{N} = \Pi CPC^T\Pi^T + \Pi N\Pi^T = \Pi\Sigma\Pi^T$. Let π_i^T be the ith row of Π. Without loss of generality, let us assume that we permute x_i and x_j to be $\tilde{x}_1$ and $\tilde{x}_2$ respectively. When examining a Granger cause from $\tilde{x}_2$ to $\tilde{x}_1$, we see that $\tilde{\Sigma}_{11} = \pi_1^T\Sigma\pi_1 = \Sigma_{ii}$ and $\tilde{\Sigma}^R$ is obtained by solving DARE with the second row of $\tilde{C}$ removed (equivalently, with the jth row of C removed.) Moreover, $\tilde{\Sigma}_{11}^R = \pi_1^T\Sigma^R\pi_1 = \Sigma_{ii}^R$. Hence, $\tilde{F}_{12} = F_{ij}$. In other words, we can just permute rows and columns of F to obtain $\tilde{F}$.

4. *If $N = 0$ and $S = 0$, then the zero pattern of F is invariant under a scaling transformation of C.* **Proof.** It is a straightforward result when solving DARE with $\tilde{C} = \beta C$ that the solution P is unchanged if $N = 0$ and $S = 0$. Moreover, $\tilde{\Sigma}_{ii}$ and $\tilde{\Sigma}_{ii}^R$ contain the same factor β^2 if $N = 0$. This makes no change in the calculation of F_{ij} in (8).

C Group-sparsity estimation of C

The problem of estimating C and A in (14) has some details of algorithm implementation. Firstly, the least-squares solution of A is obtained by $A = (V_1W^T)(WW^T)^{-1}$ and implemented by QR factorization. Secondly, when solving for C, we perform QR factorizations on problem parameters as $V_2 = R_vQ^T$ and $W = R_wQ^T$ and (14) is equivalent to

$$\underset{C}{\textbf{minimize}}\ (1/2)\|R_v - LCR_w\|_F^2 + \gamma\sum_i \|C_i^T\|_2^q \tag{24}$$

where $\beta = (\beta_1, \beta_2, \ldots, \beta_m), \beta_k \in \mathbf{R}^n$. The minimization in C, when rearrange into a vector form, falls into a regularized least-square formulation with a group norm penalty shown as

$$\underset{\beta}{\textbf{minimize}}\quad (1/2)\|y - X\beta\|_2^2 + \gamma\sum_{i=1}^m \|\beta_i\|_2^q. \tag{25}$$

The nmAPG algorithm proposed in [LL15] is applied to solve (25) which requires the proximal operator of q-norm and the Lipschitz constant of the gradient of the quadratic loss function, $(1/2)\|R_v - LCR_w\|_F^2$. It is then obtained from the following inequality:

$$\|L^TL(C_1 - C_2)R_wR_w^T\|_F^2 \le \|L^TL\|_2^2\|R_wR_w^T\|_2^2\|C_1 - C_2\|_F^2,$$

where we denote $\|\cdot\|_2$ as the spectral norm and $\|\cdot\|_F$ as the Frobenius norm of a matrix. We also have used the fact that $\|AB\|_F^2 = \|A\|_2^2\|B\|_F^2$. As a result, the Lipschitz of the gradient is given by $\|L^TL\|_2\|R_wR_w^T\|_2 = \|L\|_2^2\|R_w^T\|_2^2$, and used in a step size selection when solving (24) in the vector format.

When solving (14) with a series of γ, an explicit bound of γ can be derived so that if $\gamma \ge \gamma_c$ then the optimal solution C is entirely zero. To this end, we derive the zero-subgradient condition for (14) when $q = 1$

$$0 \in -L^T(V_2 - LCW)W^T + \gamma\begin{bmatrix} g_1^T \\ g_2^T \\ \vdots \\ g_m^T \end{bmatrix} \tag{26}$$

where g_i^T is a subgradient of $\|C_i^T\|_2$ with a known property that $\|g_i^T\|_2$ if $C = 0$. If $C = 0$ at optimum, then (26) reduces to

$$(L^TV_2W^T)_i = \gamma g_i^T, \quad i = 1, 2, \ldots, m$$

where $(L^TV_2W^T)_i$ is the ith row of $L^TV_2W^T$. Since $\|g_i^T\|_2 \le 1$ when $C = 0$, it follows that

$$\gamma \ge \max_{i=1,2,\ldots,m} \|(L^TV_2W^T)_i\|_2.$$

The critical value γ_c for (14) is therefore

$$\gamma_c = \max_{i=1,2,\ldots,m} \|(L^TV_2W^T)_i\|_2 \tag{27}$$

which depends only the problem parameters L, V_2, W and can be computed beforehand. When solving (14) with $q = 1/2$, we use a property that the non-convex penalty (when $q < 1$) often gives sparser solutions than the convex penalty (when $q = 1$) given the same γ [HTW15]. Hence, we use the same γ_c given in (27) when solving the problem with $q = 1/2$.

In contrast to sparseness property of the solutions when using $\ell_{p,q}$ penalty (15), the estimation with the ℓ_2-regularization (16) is known to gives a typically dense solution. We will show explicitly that as $\gamma \to \infty$, more weight is penalized on the norm of C and hence, $C \to 0$. As shown in Section 4.1 that the optimality condition of (14) with (16) is the Sylvester equation in C (17) of the form: $AC + CB(\gamma) = F$ where $A = L^T L$, $B(\gamma) = \gamma(WW^T)^{-1}$, and $F = L^T V W^T (WW^T)^{-1}$. This equation can be vectorized to a form of $M(\gamma)z = b$ where $z = \mathbf{vec}(C)$ and has a unique solution: $z = M^{-1}(\gamma)b$, since A and $-B(\gamma)$ have no common eigenvalues. We will show that $z \to 0$ as $\gamma \to \infty$. It can be shown that M can be represented as

$$M(\gamma) = M_1 + \gamma M_2 = \gamma M_2 (I - (-M_2^{-1} M_1)/\gamma) \tag{28}$$

where $M_1 = I_n \otimes A$ and $M_2 = B^T \otimes I_m$. If we define $G(\gamma) = -M_2^{-1} M_1/\gamma$ and if $\gamma > 1/\|M_2^{-1} M_1\|$ then $\|G(\gamma)\|_2 < 1$ and $(I - G(\gamma))^{-1}$ can be expanded by the geometric series: $[I - G(\gamma)]^{-1} = \sum_{k=0}^{\infty} G(\gamma)^k$. As a result, by properties of norm,

$$\|(I - G(\gamma))^{-1}\|_2 \le \sum_{k=0}^{\infty} \|G(\gamma)\|_2^k = \frac{1}{1 - \|G(\gamma)\|_2}. \tag{29}$$

From (28) and (29), it follows that

$$\begin{aligned} \|M^{-1}(\gamma)\|_2 &\le \|(I - G(\gamma))^{-1}\|_2 \frac{\|M_2^{-1}\|_2}{\gamma} \\ &\le \left(\frac{1}{\gamma - \|M_2^{-1} M_1\|_2} \right) \|M_2^{-1}\|_2. \end{aligned}$$

Hence, if $\gamma \to \infty$ then $\|M^{-1}(\gamma)\|_2 \to 0$ and that $\|z\| \le \|M^{-1}(\gamma)\|_2 \|b\| \le 0$. The solution $z = \mathbf{vec}\, C$ converges to zero as the penalty parameter γ approaches infinity.

D Noise covariance estimation

Consider (21) where the zero-gradient condition of the objective function is

$$h(\alpha_\eta) := f'(\alpha_\eta) = c - \mathbf{tr}((n\mathcal{A} + bI)^{-1}\mathcal{A}).$$

If the critical point of f, denoted as $\alpha_\eta^\star$ in Figure 14, is already in the interval $(0, b/a)$ then the solution of (21) is just obtained by solving $f'(\alpha_\eta) = 0$ (by any numerical methods such as a bisection). If $\alpha_\eta^\star < 0$, then minimizing f over the interval $[0, b/a]$ returns 0 as the optimal solution. In the last case, if $\alpha_\eta^\star > b/a$ then f has the minimum value on the interval $[0, b/a]$ at b/a. Therefore, we conclude that the solution of the problem (21) can be obtained from one of the following three cases.

1. If $f'(0) < 0$ and $f'(b/a) > 0$ then find the zero of $h(\alpha_\eta)$ using a bisection.
2. If $f'(0) > 0$ and $f'(b/a) > 0$ then $\alpha_\eta = 0$ and $\alpha_v = \mathbf{tr}(\Sigma_e)/r$.
3. If $f'(0) < 0$ and $f'(b/a) < 0$ then $\alpha_\eta = b/a = \mathbf{tr}(\Sigma_e)/\mathbf{tr}(LL^T)$ and $\alpha_v = 0$.

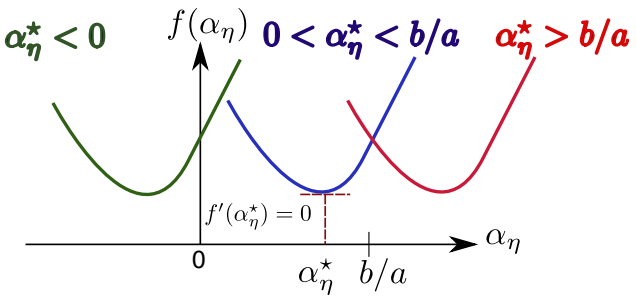

Figure 14: The problem of estimating α_η in (21) has three cases.